Surface & Coatings Technology 473 (2023) 129981

Contents lists available at ScienceDirect

Surface & Coatings Technology

journal homepage: www.elsevier.com/locate/surfcoat

Microstructural, mechanical and corrosion characterization of electroless Ni-P composite coatings modified with ZrO_2 reinforcing nanoparticles

Giulia Pedrizzetti [a,*], Laura Paglia [a], Virgilio Genova [a], Serena Cinotti [b], Michelangelo Bellacci [b], Francesco Marra [a], Giovanni Pulci [a]

[a] Department of Chemical Engineering, Materials, Environment, Sapienza University of Rome, INSTM Reference Laboratory for Engineering of Surface Treatments, via Eudossiana 18, 00184 Rome, Italy

[b] Nuovo Pignone Tecnologie Srl, Baker Hughes, Via Felice Matteucci 2, 50127 Florence, Italy

ARTICLE INFO

Keywords:
Ni-P nanocomposite coatings
Electroless plating
Nanoparticles reinforcement
Nanoparticles distribution and agglomeration analysis

ABSTRACT

This study aims to develop medium P (MP, 6 wt%) and high P (HP, 11 wt%) Ni-P-ZrO_2 nanocomposites on F22 steel substrate using an original lead-free and surfactant-free solution and to quantitatively relate nanocomposite characteristics to microhardness improvement and corrosion resistance. Incorporation, dispersion and distribution of the nanosized reinforcing phase were evaluated quantitatively by coupling Scanning Electron Microscope (SEM) imaging acquisition with original procedure for image processing and analysis. X-ray Diffraction (XRD) analysis revealed that nanoparticles introduction does not alter microstructure, which remains amorphous for HP and nanocrystalline for MP. Significant differences in particles distribution are found between MP and HP nanocomposites, which are induced by the difference in plating rate of the two formulations. Faster growth of MP (≈35 μm/h) associates with greater enveloping capability, with higher incorporation and agglomeration phenomena that result in non-uniform microhardness across the thickness. Conversely, the slower growth of HP nanocomposites coatings (≈20 μm/h) relates to lower but uniform incorporation and good dispersion of the reinforcing nanoparticles. Effective dispersion strengthening was observed for nanoparticles concentration up to 13.5 g/l. Microhardness increase by >25 % was achieved for both MP and HP coatings. The combined effect of nanoparticles incorporation level and their agglomeration was systematically studied and a mathematical model was implemented. It was demonstrated that strengthening effectiveness depends on both the amount of embedded nanoparticles and the mean size of agglomerates, following a bi-liner relation that reliably predicts experimental microhardness. Potentiodynamic corrosion test revealed that introduction of ZrO_2 nanoparticles enhance corrosion resistance of both MP and HP coatings. The presented hardening strategy for Ni-P coatings can be an efficient solution for midstream and downstream applications in the oil&gas industry, in order to increase service-life of components in contact with both wearing and corrosive media.

1. Introduction

Electroless Ni-P coatings find wide application at industrial scale to protect engineering components from environmental attack [1,2]. In the energy production sector, mild steel is extensively used as structural material because of its good machinability, mechanical strength, weldability, toughness and cost-effectiveness. Yet, typical operating environments of the oil and gas industry are rich in contaminants and erosive agents, which lead to surface degradation and accelerated failure. To extend service life of components, thick metal or alloy coatings are applied to improve wear and corrosion resistance. Historically, these coatings were produced through the easy and cost-effective electrodeposition of hard chromium from acidic Cr(VI) solutions, but their use was recently restricted for environmental and health concerns [3]. An environmentally-friendly alternative is offered by the newly proposed Cr (III) solutions, but resulting coatings are often below 10 μm in thickness, thus unsuitable for functional applications that require thicker coatings [4,5]. Another common protective approach involves applications of

* Corresponding author.
E-mail addresses: giulia.pedrizzetti@uniroma1.it (G. Pedrizzetti), laura.paglia@uniroma1.it (L. Paglia), virgilio.genova@uniroma1.it (V. Genova), serena.cinotti@bakerhughes.com (S. Cinotti), michelangelo.bellacci@bakerhughes.com (M. Bellacci), francesco.marra@uniroma1.it (F. Marra), giovanni.pulci@uniroma1.it (G. Pulci).

https://doi.org/10.1016/j.surfcoat.2023.129981
Received 10 July 2023; Received in revised form 21 August 2023; Accepted 31 August 2023
Available online 3 September 2023

hard coatings by thermal spray (e.g. Co-, Fe- or Ni-based cermet coatings, NiCr-Cr_3C_2, TiC-based compositions, etc.) [6,7]. Despite the remarkable anti-corrosion and anti-erosion properties of these coatings, thermal spray methods are costly and, being a line-of-sight process, deposition is precluded on poorly accessible internal cavities and non-visible surfaces.

In this panorama, electroless Ni-P coatings have nowadays gained attention thanks to their excellent wear and corrosion resistance, hardness and solderability [8–10]. The electroless plating process involves the controlled reduction of metal ions onto a catalytic substrate by a reducing agent in solution, without requiring external current. This enables the production of dense, uniform, and conformal coatings on any surface in contact with the plating solution, regardless of shape or geometry [11].

Microstructure of Ni-P alloys depends on phosphorus content: low P (1–5 wt%, LP) results in crystalline structures, medium P (6–9 wt%, MP) produces mixed amorphous-crystalline, and high P (10–13 wt%, HP) leads to completely amorphous structures [12–14]. Corrosion resistance improves with higher P content, while hardness increase is linked to the crystalline structure typical of lower P content [15,16].

When the expected applications are particularly demanding, hardness and tribological properties of the coatings can be enhanced by the introduction of hard second-phase particles, which hinder the fast propagation of dislocations in the ductile Ni matrix by dispersion hardening [17]. Second phase inert particles can be easily embedded in the coating during the electroless process, since they are readily dispersed in the plating solution. According to the model proposed by Ger et al. [18], particle incorporation proceeds through a multi-step mechanism: (1) inert particles are transferred from the bulk solution towards the substrate by means of forced convection, (2) they are loosely adsorbed onto the cathode surface and, (3) given sufficient residence time, they are irreversibly incorporated into the growing Ni-P matrix. Mechanical properties of the composite coating are strongly influenced by particles size and incorporation level [19–21]. The use of finely dispersed nanoparticles, which can be easily kept in suspension, can aid their adsorption onto the substrate and incorporation within the growing coating. Strengthening induced by nanoparticle introduction can be explained by two mechanisms: (i) load bearing effect of the reinforcement; (ii) hindering of dislocation motion by Orowan mechanism [22–24]. As extensively studied by Zhang et al. [25,26], the Orowan mechanism's contribution to strengthening increases with decreasing reinforcing phase size and effective improvement of mechanical properties is expected when well dispersed nanoparticles are incorporated in the coating. Consequently, several researches were focused on synthesizing nanocomposite coatings reinforced with various ceramic nanoparticles such as SiC [27–30], Si_3N_4 [31,32], Al_2O_3 [33–35], TiO_2 [36–38], TiN [39,40], HfC [41].

Among the proposed compounds, ZrO_2 stands out as a promising reinforcing phase due to its toughness, strength, hardness, and chemical resistance [42]. Additionally, high ζ-potential of ZrO_2 allows the easy preparation of well-dispersed and stable suspensions, making it an ideal candidate for manufacturing of nanocomposite coatings [43]. State-of-the-art analysis demonstrates that approaches based on modification with zirconia holds promise in various applications [44–50]; however, some co-deposition challenges hinder its standardization. First, effectiveness of reinforcement is strongly affected by nanoparticles quantity and dispersion (i.e. size of agglomerates). These parameters are crucial for the optimization of coating properties, but their assessment is not straightforward. Second, it is difficult to obtain nanocomposite coatings with satisfying dispersion and distribution of the reinforcing phase without using surfactants, but introduction of additives can affect coating characteristics in terms of composition, properties, internal stresses and microstructure [51–53], making it difficult to opportunely control coating properties.

A potential approach for quantitative evaluation of particle incorporation utilizes quantitative image analysis (QIA). Initially introduced in the context of Ni-P composite coatings by Bozzini et al. [54], QIA enables particle identification through compositional contrast differences between the matrix and the reinforcing phase. Consequently, its applicability has often been limited to particles giving high contrast level with the Ni-P matrix. Examples include Al_2O_3 [55–59], SiC [21,60,61], WC [62], Si_3N_4 [63], BN [64], Diamond [54,65], and Ag [59].

Identification of a versatile technique to quantitatively assess both nanoparticle incorporation and dispersion is of utmost importance in determining coating properties. To the authors knowledge, a method for enhancing QIA's applicability and evaluating the combined effect of these two microstructural features is still not available in literature.

This work focuses on the manufacturing of Ni-P-nanoZrO_2 coatings using an original surfactant-free solution and aims to quantitatively relate particle incorporation and agglomeration to microhardness improvement and corrosion resistance (without the influence of any additive). To do this, a novel and versatile routine for image processing and analysis was developed, capable of identifying nanoparticles with low compositional contrast with the NiP matrix. Thanks to this new QIA approach, MP and HP coatings with different concentrations of ZrO_2 nanoparticles were manufactured and the amount of incorporation, dispersion and distribution of the nanosized reinforcing phase were quantitatively evaluated to provide an objective assessment of nanocomposite features. A new mathematical model was implemented to correlate the proposed nanocomposite parameters to strengthening, thus providing a method for the choice of deposition parameters that help maximizing hardness improvement. Eventually, potentiodynamic polarization tests were then conducted on optimized coatings to clarify the effect of P content and ZrO_2 introduction on the corrosion behavior.

2. Materials and methods

2.1. Coating preparation

Square-shaped specimen made of ASTM 182 F22 steel with square shape, measuring 15 mm × 15 mm × 3 mm, served as the substrates for the experimental activity. Chemicals from Sigma Aldrich (Merck KGaA) were used without additional purification. Surface pre-treatment was done following the ASTM international designations B 183-79, B 322-99, and B 733-97. As first step, substrates were immersed in a NaOH solution (1 molar concentration) at 80 °C for 10 min, to remove any residual of machining lubricants and liquids for storage. Second, sandblasting was performed using corundum (mesh 80) as abrasive material, in order to remove contaminants, increase surface roughness and promote deposition. Last, samples were activated with a 50 vol% diluted solution of HCl 37 wt% by immersion for 1 min at room temperature. This step guarantees the removal of any oxide residual that may hamper deposition by reducing the exposed autocatalytic surface. Each cleaning step was followed by rinsing in deionized water.

Electroless solutions were prepared using a lead-free recipe, where concentration of reagents was varied according to the amount of

Table 1
Composition of the plating solutions for deposition of MP and HP coatings.

Compound	Function	MP (g/l)	HP (g/l)
Sodium hypophosphite	Reducing agent	70	110
Sodium acetate	Buffer	15	20
Citric acid	Chelating Agent	6	9
Nickel sulphate	Source of Nickel	12	25
Thio-organic compound	Stabilizer	5 ppm[a]	8.5 ppm[a]
Nano-ZrO_2	Reinforcing phase	0 (MP)	0 (HP)
		4.5 (MPZ-1)	4.5 (HPZ-1)
		9 (MPZ-2)	9 (HPZ-2)
		13.5 (MPZ-3)	13.5 (HPZ-3)

[a] The stabilizer was added by liquid solution (1 mol/kg) and respecting the quantity in ppm.

phosphorus to be deposited. Detailed composition of the plating baths for the MP and HP depositions is reported in Table 1. According to the proposed recipes, MP and HP solutions produce Ni-P coatings with a P content of ≈6 wt% and ≈11 wt%, respectively. P content was evaluated from EDS analysis on selected cross-sectional areas centered at half of coating width and comprising 80 % of total thickness. Electroless plating was carried out at 90 °C in a beaker under magnetic stirring and constant control over temperature. Before immersing the substrates, solutions were heated to the deposition temperature using an IKA™ RET Control-Visc hot plate equipped with an external temperature sensor. Pre-heating is necessary to guarantee correct activation and uniformity of the process. pH value was set to 4.2 and monitored using a METTLER TOLEDO™ Seven Excellence pH-meter model S400, equipped with pH sensor InLab® Viscous Pro-ISM.

Commercial ZrO_2 nanoparticles, with a particle size ranging between 50 and 100 nm, were supplied by IoLiTec (Ionic Liquid Technologies GmbH, Heilbron, Germany) and used without any further purification. The SEM micrograph of as-purchased nanoparticles is reported Fig. 1(a). Mean size of nanoparticles was measured by Dynamic Light Scattering (DLS) using the Plus 90 instrument supplied by Brookhaven. Mean diameter is 74.9 nm and nano-ZrO_2 particle size distribution is shown in Fig. 1(b). Powders were added to aqueous solutions to get a final concentration of 4.5 g/l, 9 g/l and 13.5 g/l. Such range of concentration (4.5–13.5 g/l, average size ≈ 75 nm) was selected to obtain a specific surface area of nanoparticles in solution comparable to those providing the best results (1–8 g/l, average size 5–35 nm), according to literature state of the art [46,47,50,66,67]. To promote dispersion, nanoparticles suspensions were sonicated with Elmasonic S 30 (H) ultrasonic bath with ultrasonic frequency of 37 kHz and ultrasonic power effective of 80 W for at least 15 min. Sonicated suspensions were added to the plating solution 10 min after beginning of deposition, to avoid any activation issue. Plating time was 90 min for both standard and nanocomposite coatings using a bath loading of 55 ml/cm^2. Characteristics of all the produced samples are summarized in Table 2, MP and HP coatings with increasing concentration of nano-ZrO_2 are addressed as MPZ-1, MPZ-2, MPZ-3 and HPZ-1, HPZ-2, HPZ-3, respectively.

Table 2
Coating characteristics. MP and HP coatings with increasing concentration of nano-ZrO_2 are addressed as MPZ-1, MPZ-2, MPZ-3 and HPZ-1, HPZ-2, HPZ-3.

Sample	P content (wt%)	n-ZrO_2 in plating solution (g/l)
MP	≈6 %	/
MPZ-1	≈6 %	4.5
MPZ-2	≈6 %	9
MPZ-3	≈6 %	13.5
HP	≈11 %	/
HPZ-1	≈11 %	4.5
HPZ-2	≈11 %	9
HPZ-3	≈11 %	13.5

2.2. Coating characterization

Surface morphology, thickness and composition of the coatings, as well as nanoparticles dispersion and distribution, were determined by a FEG-SEM Tescan Mira3 (Tescan, Brno, Czech Republic) equipped with Edax Octane Elect EDS system detector (Edax/Ametek inc.) for energy-dispersive X-Ray spectroscopy (EDS); Edax Team v.4.5 software was employed for the elementary analysis. Samples were prepared for cross sectional analysis by mounting in epoxy resin, cutting with a linear precision saw with BCN cutting disc and polishing with SiC papers (grit from P400 to P1200) and water-based diamond suspensions (from 9 μm to 1 μm).

X-ray diffraction analysis (XRD) was performed with a Philips X'Pert diffractometer (PANalytical BV, The Netherlands), operating at 40 KV and 40 mA with CuKα1 radiation, with scan range of 20–80° (2θ), feed step of 0.02° and acquisition time of 2 s. The microstructural characteristics of standard and nanocomposite coatings were investigated as a function of phosphorus and nanoparticle incorporation and the crystallite size was calculated using Scherrer's equation [68]:

$$D = \frac{0.94\lambda}{\beta\cos(\theta)}, \quad (1)$$

where λ is the wavelength of the radiation used, β is the half-maximum width and θ is the position of the main peak. No correction for instrumental broadening was made.

The presence of through the thickness cracks and defects induced by coating growth stress was investigated by the Ferroxyl reagent test (ASTM B689-97). The test is designed to detect iron contamination on the surface of components and it is based on the reaction of potassium ferrocyanide with iron is a strongly acid medium: the iron dissolves in the strongly acid medium as Fe^{2+} to form a blue complex that can be easily detected by visual analysis. During the test, a filter paper is moistened with some drops of the Ferroxyl solution and placed on the surface of the coated samples: if a blue coloring becomes visible, some of the solution managed to reach the steel substrate, revealing the presence of through-the-thickness porosities or cracks.

2.3. Image processing and analysis

Nanoparticles concentration in the coating and their dispersion were determined acquiring cross sectional SEM images and analyzing them with an original procedure for image processing and analysis implemented in MATLAB (v. 2021b, The MathWorks Inc.). The main steps for recognizing ZrO_2 nanoparticles from the surrounding NiP matrix are listed below and presented in Fig. 2:

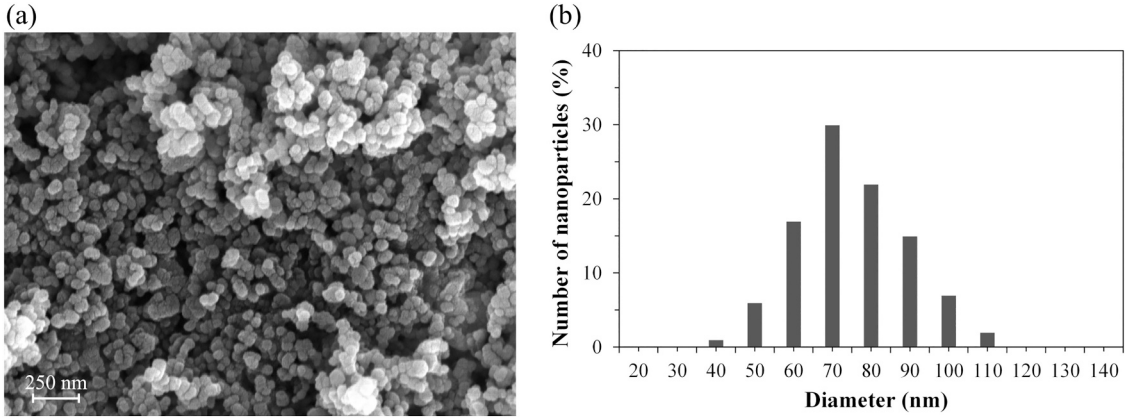

Fig. 1. SEM micrograph of as-purchased ZrO_2 nanoparticles (a) and particle size distribution measured by DLS (b).

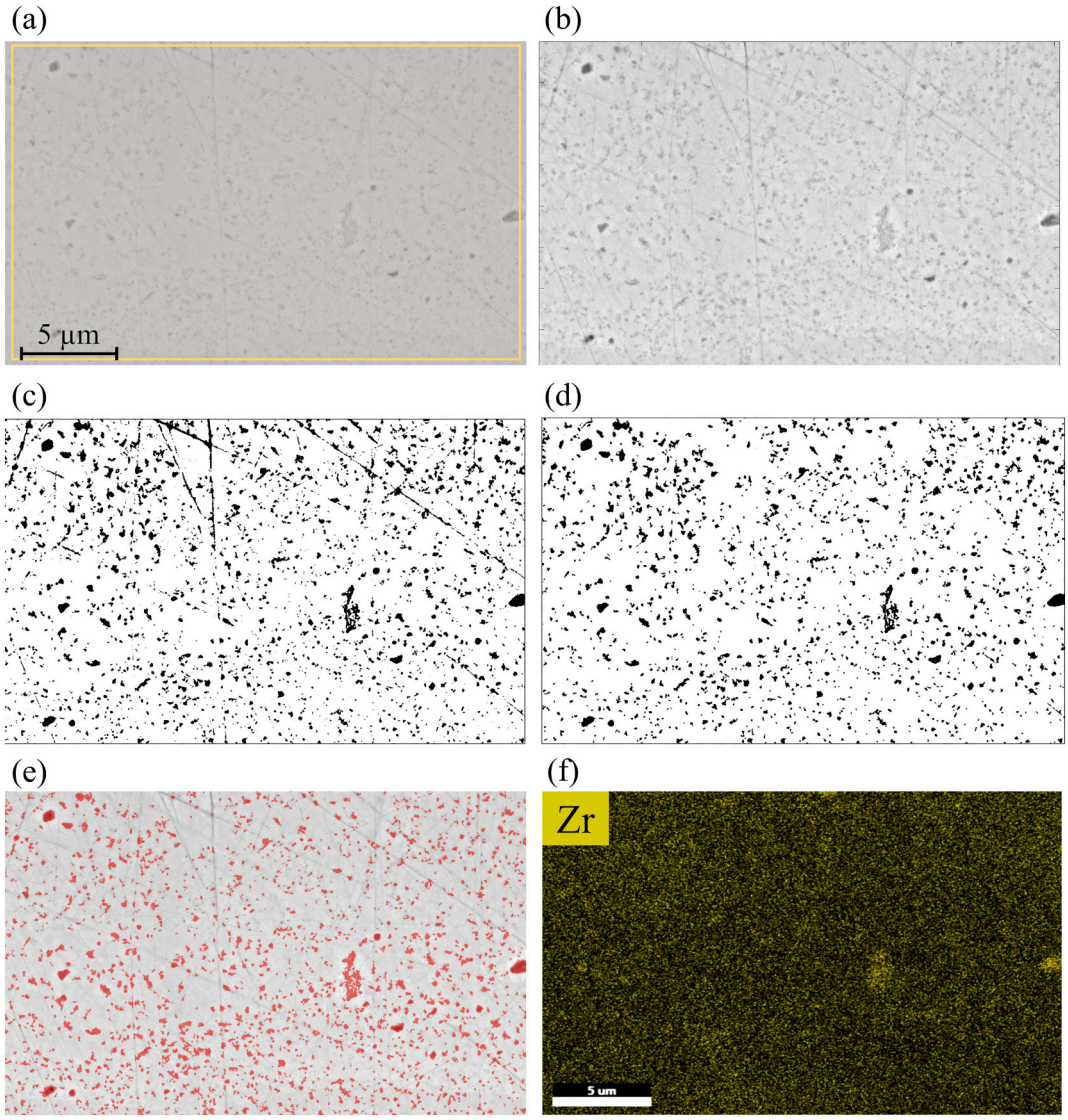

Fig. 2. Main steps of the image processing and analysis routine for the identification nanoparticles: (a) ROI selection from the original SEM image; (b) application of the Gaussian filter and sharpening; (c) binarized image where black regions represent particles and scratches; (d) image after filtering of scratches; (e) routine output, with red spots corresponding to nanoparticles superimposed on the SEM micrograph; (f) EDS map of Zr element.

1. The region of interest (ROI) is selected from the SEM picture (Fig. 2a);
2. A 3 × 3 Gaussian filter is applied to remove small scale noise and a sharpening procedure is performed to enhance definition of nanoparticles (Fig. 2b);
3. Image is made binary according to a proper color threshold in the grayscale: nanoparticles, which appear darker in the original image thanks to the compositional contrast of BSE acquisition, turn black and are easily identified from the NiP matrix, which turns white (Fig. 2c);
4. A critical aspect of step 3 is that polishing scratches originated from the metallographic preparation are often deep and the darker areas of topological contrast cannot be differentiated from the compositional contrast of ZrO_2. To overcome this limit, the last step involves application of a filter that differentiates black areas according to their aspect ratio. Scratches, which are characterized by a more elongated shape, are removed and only nanoparticles are left in black for analysis (Fig. 2d).

The routine output is reported in Fig. 2e, where red spots corresponding to ZrO_2 are superimposed on the original SEM picture to demonstrate the good matching. As a comparison, Fig. 2f shows Zr distribution detected by EDS map: Zr signal is present all across the coating, but only bigger particles or agglomerates can be precisely identified due to the relatively low spatial resolution of EDS, which is commonly limited to 1 µm for Ni-P specimen at accelerating voltage of 15–20 kV [69]. Conversely, nanoparticles can be precisely recognized by the image analysis routine, whose resolution corresponds to the one of BSE-SEM image acquisition.

Increased flexibility of the proposed method makes QIA applicable to a wider range of particles, including those giving low contrast with the matrix. Moreover, step 4 of the routine increases reliability of results, which are made independent from possible artifact or defects that originate from the preparation of samples. The precise identification of the reinforcing phase allows assessment of the fundamental nanocomposite features, namely the percentage of incorporated nanoparticles, calculated as the ratio between the total area of nanoparticles and the area of the ROI, and the particle size distribution of the embedded reinforcement. This last parameter, when compared to the mean size of purchased nanoparticles, is representative of agglomeration: the ratio between measured particle size and mean size (75 nm) provides the average number of agglomerated particles. The combined

effect of these two parameters on coating hardness was investigated with a mathematical method based on experimental data fitting procedures.

2.4. Microhardness

Microhardness of the coatings was evaluated according to ASTM E384-11 using a Leica VMHT (Leica GmbH, Germany) with a Vickers diamond indenter under a load of 50 gf and indentation time of 15 s. Distance between two indentations was ≥50 μm and measurements were performed on cross-sections. Coating hardness was investigated for the as-coated samples with different phosphorus content and different concentration of ZrO_2 nanoparticles. Results on each of the examined regions report the average value and standard deviation of at least twenty repeated measurements.

2.5. Potentiodynamic polarization test

Influence of P content and ZrO_2 introduction on the corrosion behavior of samples was studied by potentiodynamic polarization technique with a three-electrode system, according to ASTM G59-97 standard (as indicated by specification B733-04) [70]. Three-electrode setup consisted of the specimen with unit exposed area as the working electrode, saturated standard calomel electrode (SCE) as the reference electrode and platinum mesh as the counter electrode. Tests were performed at 20 °C in open air in a cell containing 3.5 wt% NaCl solution using a PARSTAT 3 potentiostat/galvanostat (Princeton Applied Research) with scan rate of 0.1666 mV/s within the potential range of −0.200 V to +0.450 V with respect to the Open Circuit Potential (OCP). Samples were immersed in testing solutions 30 min before starting analysis and OCP was measured for 1800 s. The Tafel extrapolation of polarization curves was used to determine the corrosion potential (E_{corr}) and corrosion current density (I_{corr}). Polarization resistance R_p was measured using Stern-Geary simplified equation [71]:

$$R_p = \frac{\beta_a \cdot \beta_c}{2.303 I_{corr}(\beta_a \cdot \beta_c)}, \quad (2)$$

where β_a and β_c are the anodic and cathodic Tafel slopes, respectively.

3. Results and discussion

3.1. Morphology and phase composition

Surface morphology of MP and HP coatings reinforced with different concentration of nano-ZrO_2 are showed in Fig. 3. Both unreinforced and nanocomposite coatings exhibit the classical nodular morphology of electroless Ni-P coatings, with smaller nodular size for HP coatings. It is known that, during coating formation, phosphorus tends to gather at Ni grain boundaries, and both microstructural and morphological features depend on P content [72]. Smaller nodules of HP coatings form as a consequence of the higher P amount, that limits growth of Ni grains and increases the number of nucleation sites. In addition, nanoparticles introduction also plays a role on morphology and both MP and HP nanocomposites are characterized by a more refined nodular structure respect to their standard counterpart. This might be caused by the incorporation of the nanosized reinforcing phase, which limit lateral growth of the single nodules, as also reported elsewhere [47,73]. However, no particular difference in nodular size was detectable from top view images of nanocomposite coatings reinforced with difference concentration of nano-ZrO_2 (Fig. 3b, c and e, f). This is in contrast with the results report by Sliem et al. [48], where a progressively more refined structure was observed for increasing concentration of nanoparticles.

XRD studies reported in Fig. 4 confirm that coatings containing higher quantity of phosphorus are characterized by an amorphous profile. A single broad peak corresponding to Ni (111) is located at an angular position ranging between 35 and 55° and the calculated average crystallite size below 2 nm. This value can only be considered as qualitative and it indicates that HP coatings have an amorphous microstructure, which originates from the Ni lattice distortion induced by the high amount of P atoms situated in interstitial positions [74–76]. Conversely, the quantity of phosphorus contained in MP coatings (≈6 wt %) is only sufficient to create small pockets of amorphous nickel, resulting in a nanocrystalline structure. Initial Ni (200) and Ni (220) peaks can be identified from MP and MPZ-3 spectra and average grain size, calculated by the Scherrer formula, is approximately 2.7 nm for both particle-free and nanocomposite. Grain size measurements strongly agree with those reported in literature for coatings with comparable P

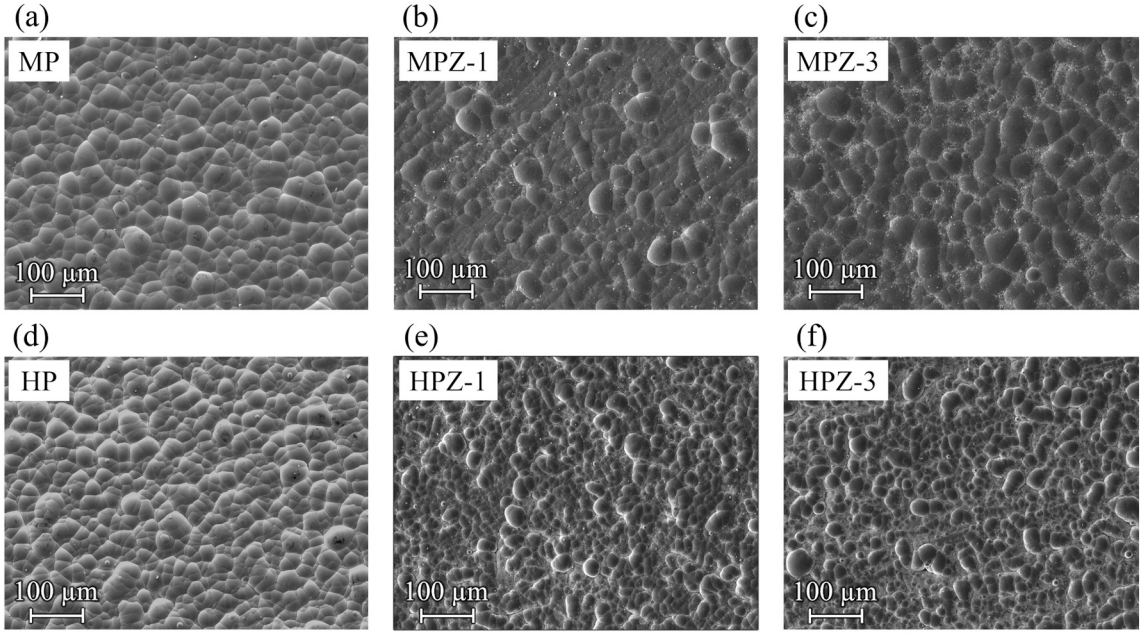

Fig. 3. Surface morphology of different NiP coatings: (a) bare MP (b) MPZ-1, reinforced with 4.5 g/l of nano-ZrO_2; (c) MPZ-3, reinforced with 13.5 g/l of nano-ZrO_2; (d) bare HP; (e) HPZ-1, reinforced with 4.5 g/l of nano-ZrO_2; (f) HPZ-3, reinforced with 13.5 g/l of nano-ZrO_2.

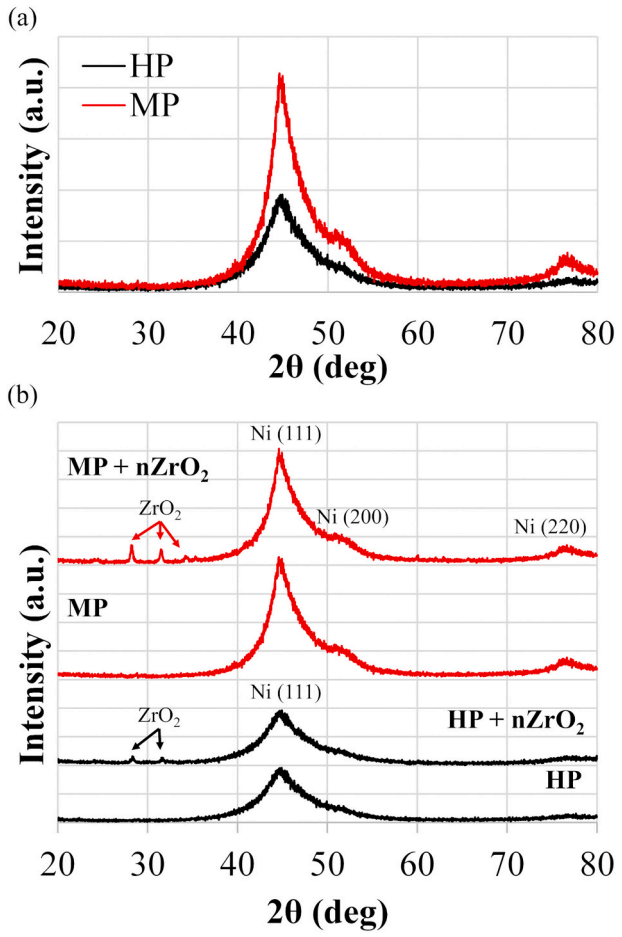

Fig. 4. Comparison between XRD spectra of standard and nanocomposite NiP coatings.

amounts [27,68,77]. The only difference between particle-free and nanocomposite coatings is given by the additional peaks located at 2θ positions 28.2° and 31.5° and corresponding to ZrO_2, which indicate the presence of nanoparticles. This suggests that incorporation of the reinforcing phase does not alter microstructure of the NiP matrix, as similarly reported by other authors after incorporation of different types of particles [12,27,78]. MP nanocomposites show relative higher intensity of ZrO_2 peaks compared with HP ones and an additional small peak at 2θ position of 34.3° can be identified. This suggests an incremented co-deposition of nanoparticles, despite the same concentration in the plating solution. This effect will be further discussed in the next paragraphs. Fig. 5 shows a comparison between XRD spectra of HPZ-1 and HPZ3 (a) and MPZ-1 and MPZ-3 (b). The produced nanocomposites share the same diffraction pattern, with relative intensity of the ZrO2 peaks that decreases for decreasing concentration of nanoparticles in the plating solution.

No peaks that can be attributed to the substrate are identified in the analyzed XRD spectra and all samples are successfully tested negative to Ferroxyl reagent test, indicating the absence of through-the-thickness defects that could prejudice both corrosion resistance and mechanical properties.

3.2. Cross section analysis

HP coatings are characterized by a lower thickness compared with coatings with medium phosphorus content, despite the same deposition time (90 min). Slower plating rate of HP deposition is mainly attributed to the lower amount of $NiSO_4$ present in the plating solution (−45 wt% compared to MP formulation). The decreased concentration of nickel salt is a key factor for increasing the content of co-deposited P, but the lower amount of Ni^{2+} ions available for reduction also corresponds to a dramatically slower deposition [79]. Nevertheless, this is not considered a limitation since specific thickness requirements can be easily met by varying the deposition time. Mean thickness of standard and nanocomposite coatings, measured directly from SEM images, are reported in Fig. 6: nanocomposite coatings present comparable or higher thickness respect to bare Ni-P coating, indicating a higher deposition rate. In MP nanocomposites, a slight increase in plating rate can also be observed with increasing concentration of ZrO_2 nanoparticles in the bath. A

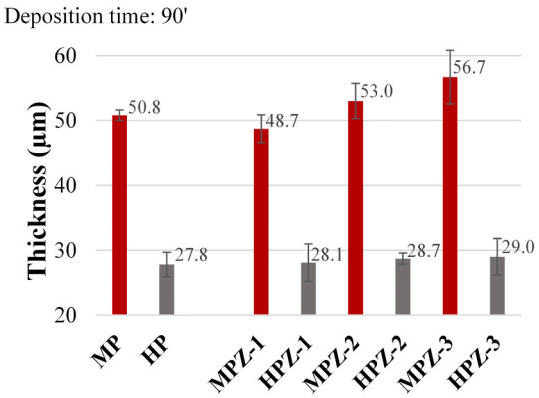

Fig. 6. Thickness of MP and HP coatings with different amount of nano-ZrO_2 addition in the plating solution after 90′ of deposition.

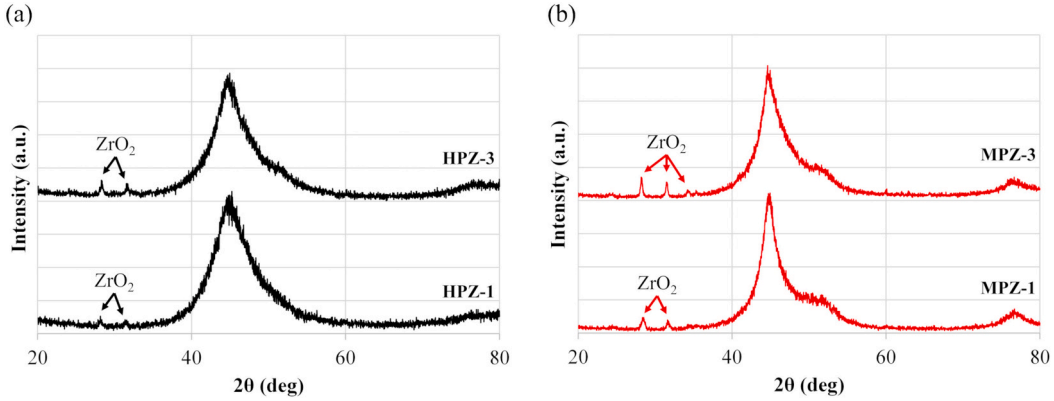

Fig. 5. XRD spectra of HPZ-1 and HPZ3 (a) and MPZ-1 and MPZ-3 (b) showing the decreasing intensity of ZrO_2 peaks according to the decreasing concentration of nanoparticles in the plating solution.

similar increase in the plating rate upon addition of nanoparticles in the plating solution was observed by several other authors [80–82]: the large surface area of nanoparticles, that are easily adsorbed and co-deposited in the nucleating NiP layer, may enhance surface activity and increase the number of nucleation sites that are catalytically active for deposition, thus increasing the rate of deposition [17,83]. Conversely, the thickness of HP coating remains barely constant irrespective of the amount of nanoparticles in the plating bath. Such different behavior might be explained by the generally slower plating rate of HP coating, equal to ≈20 μm/h, compared with MP ones, which grow with ≈35 μm/h rate: the globally lower number of active nucleation sites of HP deposition and the higher concentration of stabilizer in the plating solution probably decreases the surface activity [84,85], so that the effect of nanoparticles on plating rate becomes hardly evident.

Low energy back-scattered electrons (LE-BSE) cross sectional SEM micrographs of HP and MP standard and nanocomposite coatings reinforced with different concentration of nano-ZrO_2 are reported in Fig. 7. EDS analysis confirms that 6.4 ± 0.35 wt% and 10.8 ± 0.35 wt% of P is present in MP and HP coatings, respectively, and panels of Fig. 7 show effective embedding of ZrO_2 within the coatings (only EDS of MPZ-2 and HPZ-2 samples is reported, but they are representative of all MP and HP nanocomposites). Due to the very small size of particles and the low compositional contrast between the NiP matrix and ZrO_2, it is difficult to precisely individuate the reinforcing phase from unprocessed LE-BSE SEM images and EDS maps. Nevertheless, three observations can be readily done: (*i*) a lower concentration of nanoparticles in the plating solution corresponds to a lower level of incorporation into the matrix for both MP and HP coatings; (ii) a higher amount of nanoparticles is embedded in MP coatings respect to HP ones for any concentration of ZrO_2 in the plating solution; (*iii*) nanoparticles are not uniformly embedded across the thickness, with higher concentration of particles localized near the substrate, especially for MP coatings. To better explain observation (*iii*), Fig. 8 shows MPZ-3 (a) and HPZ-3 (b) coatings divided into three different regions, addressed as inner, near the substrate, central and outer. It is evident that a high quantity of agglomerated particles is present in the inner region of MPZ-3 coating and the amount of embedded nano-ZrO_2 progressively decreases towards the outer region. A more uniform distribution can be observed in HPZ-3 coating, even though the quantity of embedded nanoparticles seems considerably lower.

The quantitative analysis of the amount of nanoparticles (expressed as a fraction of area, A%) embedded in the NiP matrix of each coating as a function of the distance from substrate is reported in Fig. 9. As expected, a different initial concentration of nanoparticles in the plating solution corresponds to a higher A%. In fact, a higher availability of nanoparticles close to the substrate allows a more efficient entrapment in the forming matrix [77]. Nevertheless, a steep decrease in the incorporation yield can be registered for all MP nanocomposites after formation of the first 10–15 μm of the coating. Conversely HP nanocomposites are characterized by a more uniform distribution of nanoparticles across the thickness, with only a small decrease in the incorporation level in the outer region. This different behavior cannot be ascribed to the consumption of suspended nanoparticles in the plating solution since the embedded amount in all coatings is of the order of milligrams, which is much lower than the availability in the plating solutions (order of grams). The decrease in A% of particles along with coating growth for MP nanocomposites can be partially explained by the formation of clusters in the plating bath. Typically, particles in the plating solution are covered by an ionic cloud and are transported to the substrate by means of convection and diffusion and naturally tend to agglomerate due to their extremely large surface energy [86]. This fact cannot be avoided completely by stirring and, as the deposition proceeds, agglomeration takes place to decrease the global free energy of the system. Agglomeration in the plating solution leads to both agglomeration of the reinforcing phase in the coating and a reduced yield of incorporation, since the entrapment adhesion of bigger clusters is lower [87–89]. This interpretation is confirmed by the steeper decrease in incorporation registered for MPZ-3 coatings, which presented the higher concentration of nanoparticles in the plating solution (i.e. the lower mean distance between suspended particles that increases their chance to agglomerate). Several authors dealt with the problem of agglomeration and resorted to the use of surfactants to enhance particle dispersion [43–45]; yet, the use of surfactants or additives are known to affect characteristics and properties of the produced coatings (e.g. composition, internal stresses and microstructure [43,66,90–92]) and it was chosen to not use them in the present work.

The phenomenon discussed above is only partially appliable to HP nanocomposite coatings, which exhibit a completely different trend of the amount of nano-ZrO_2 along the coating thickness compared with MP. Indeed, they show a considerably lower amount of nanoparticles embedded within the NiP matrix and a more uniform distribution across the thickness. Given that nanoparticles concentration within the plating solution is the same, the difference can only be imputable to the bath formulation, that is known to highly affect the deposition process and the coating characteristics [11,19,77]. The difference between MP and HP plating baths can be expected to influence the rate of incorporation, as can be verified by comparing the plating rate curves reported in Fig. 10. Considering that the electroless co-deposition process involves the impingement and settling of nanoparticles onto the surface of the sample and their subsequent entrapment in the metal layer as it is deposited, a faster forming NiP matrix guarantees a higher level of incorporation. The faster rate of MP deposition implies a superior enveloping capability and a shorter residence time is sufficient to embed the reinforcing phase. The slower growth of HP coatings is only capable of entrapping small clusters, giving quantitative smaller but more homogeneous distribution of the reinforcement across coating thickness. The progressive decreasing of highly dispersed nanoparticles, therefore, also explains the slight decrease of A% observed only in the outer region of HP nanocomposites coatings.

For the sake of clarity, it must be remarked that the image analysis process allows identification of the area occupied by nanoparticles as a fraction of the total area of the analyzed cross section. However, according to Sahagian and Proussevitch [93], when the aspect ratio of embedded particles is close to unity, the 2D area fraction can be assumed to be equal to the 3D volume fraction.

The similar amount of nanoparticles present in the outer region of MP and HP coatings, regardless of the initial concentration in the plating solution, also explains the similar morphology observed, respectively, all the three types of MP and HP nanocomposites, which exhibited comparable size of nodules.

3.3. Microhardness

Fig. 11 shows the effect of nano-ZrO_2 concentration in the plating bath on microhardness of MP and HP coatings. The general lower hardness of HP coatings can be explained by the smaller grain size (<2 nm) associated to the higher P content. For grain size up to 15 nm, deformation processes are governed by grain boundary sliding and rotation [61], according to the *reverse* Hall-Petch effect [94]. Smaller grain size corresponds to a higher number of triple junctions relative to the volume fraction of grain boundaries, with detrimental effects on microhardness. Thus, medium phosphorus coatings with higher grain size and lower triple junction fraction have higher hardness compared to high phosphorus ones. Introduction of nanoparticles causes microhardness increase for both MP and HP coatings. Higher concentration of nanoparticles in the plating solution corresponds to higher hardness, with values up to 715 HV_{50} for MPZ-3 and 674 HV_{50} for HPZ-3 samples. The strengthening mechanism of the reinforcing phase effectively takes place and nanoparticles act as a barrier to dislocation motion, hindering their easy sliding in the ductile NiP matrix and increasing hardness.

It is important to point out that Fig. 11 only reports average values of microhardness and does not consider its variability across the thickness

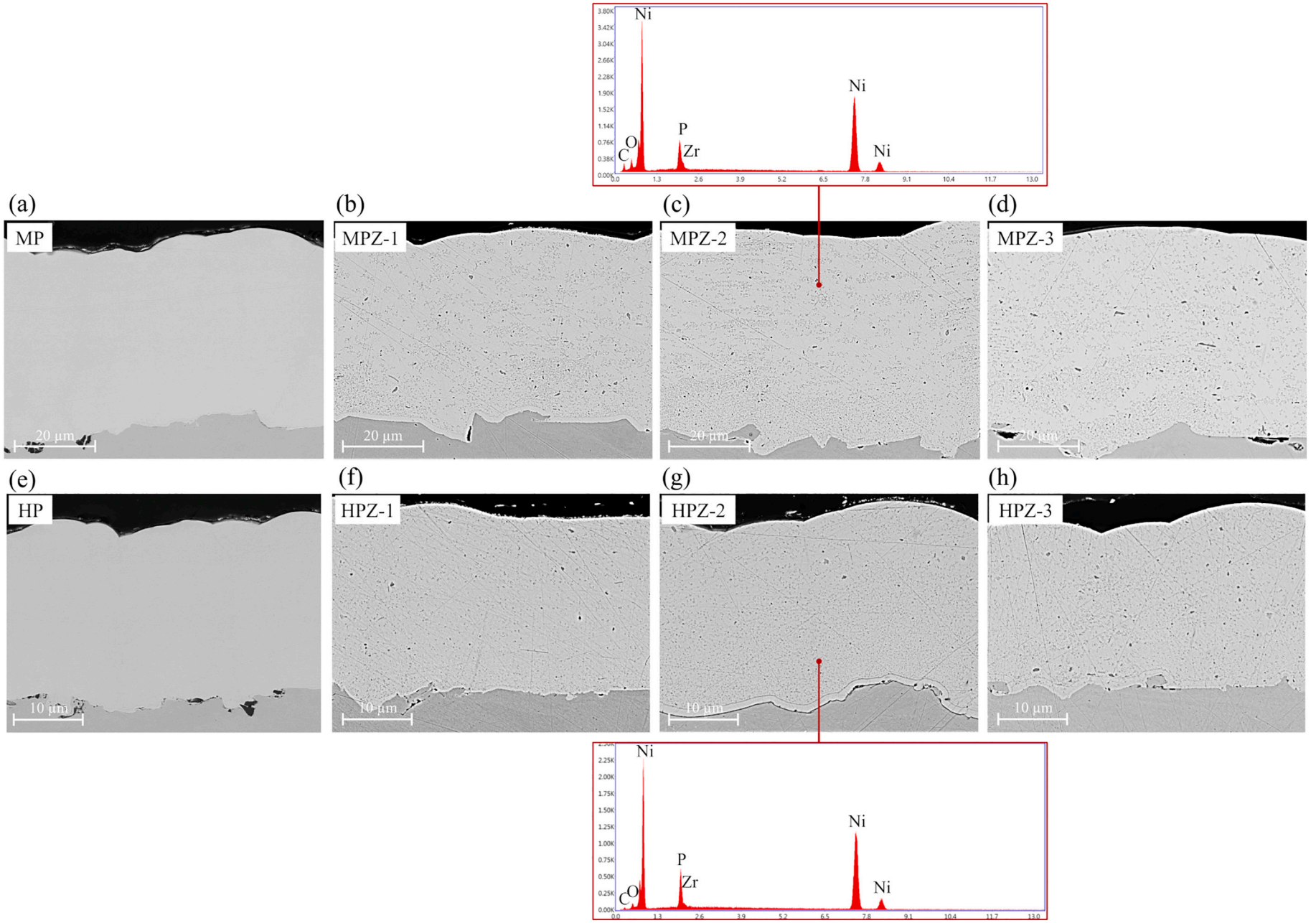

Fig. 7. Cross sectional SEM micrographs of MP (a, b, c) and HP (a, b, c) coatings reinforced with different concentration of nano-ZrO_2. EDS analysis demonstrates presence of ZrO_2 only in the NiP matrix and is representative of all coatings.

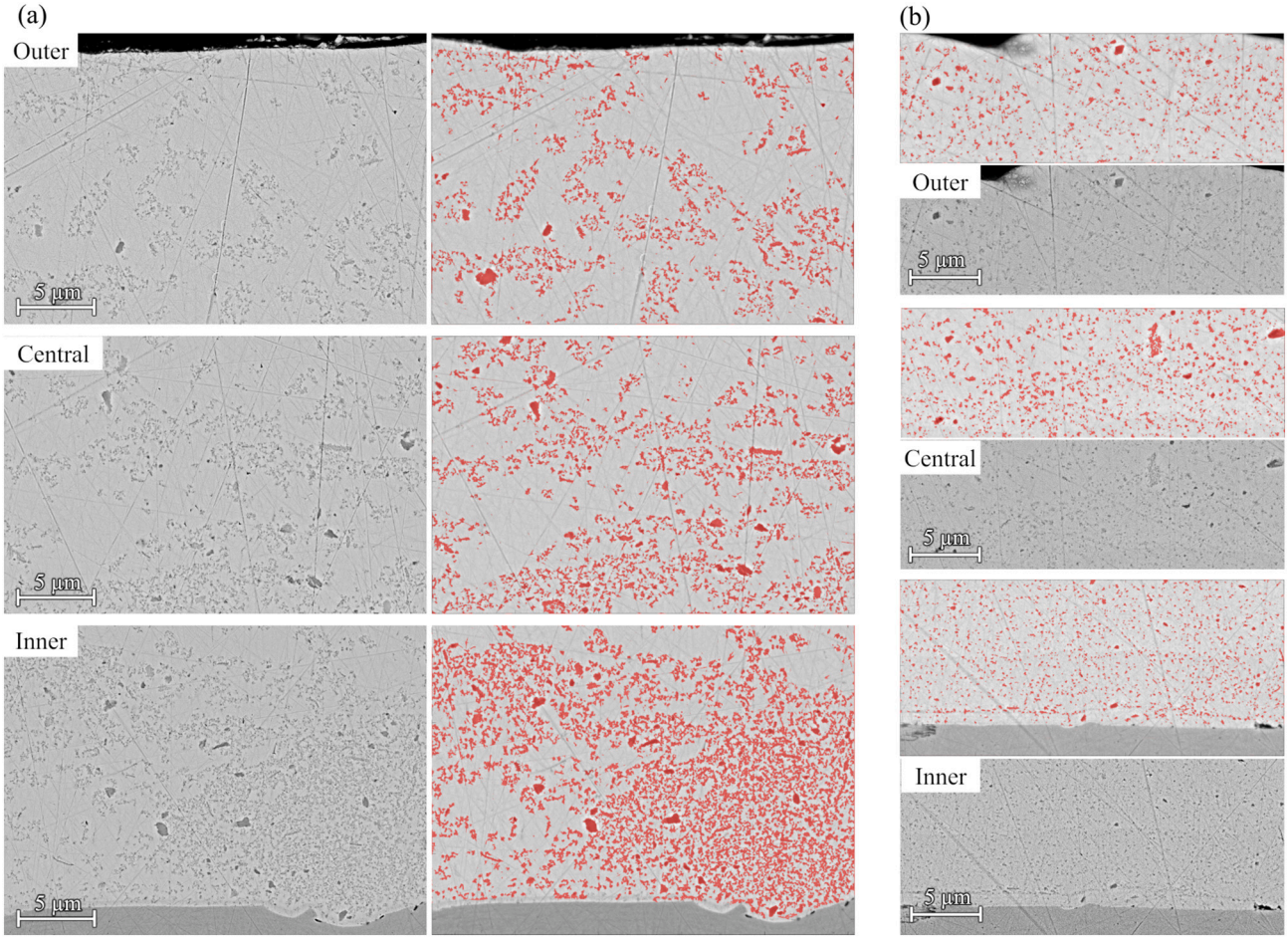

Fig. 8. High magnification LE-BSE SEM micrographs showing incorporation of nano-ZrO_2 in the inner, central and outer regions of the same coatings: (a) MPZ-3, original SEM image on the left, output of the particle identification routine on the right; (b) HPZ-3, original SEM image on bottom, output of the particle identification routine on top.

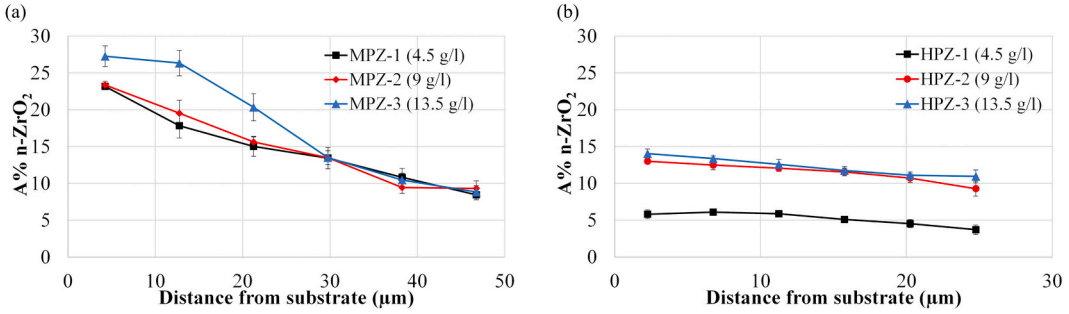

Fig. 9. Curves showing quantitative analysis of the amount of embedded ZrO_2 nanoparticles (expressed as a fraction of area, A%) as a function of the distance from substrate for (a) MP nanocomposites; (b) HP nanocomposites.

that can arise from a non-uniform distribution of the reinforcing phase. To uncover this aspect, Fig. 12 shows microhardness measured in the inner, central and outer regions of the nanocomposites: as expected, MPZs present non-uniform hardness, that progressively decreases towards the outer zone. This decrease is small for MPZ-1 coating and it is more marked for MPZ-2, whereas MPZ-3 exhibit a maximum in the central region. Differently, all HP nanocomposites exhibit a similar trend with only a slight microhardness decrease with comparable slope, irrespective of ZrO_2 concentration in the bath. These trends are even more evident from Fig. 13a, that represent the relative hardness increase of nanocomposites, ΔHV_{50}, in terms of increment with respect to the unreinforced coatings.

The principal factors affecting effectiveness of reinforcement are (*i*) the A% of embedded ZrO_2, that must be high for good reinforcement and (*ii*) the average size of the embedded agglomerates (expressed as the mean number of particles per agglomerate, n_a, that is inversely related to dispersion), the lower the better. These two parameters were separately calculated in each region by means of image analysis, and the relative curves are reported in Fig. 13b and c (error bars are not reported in the graphs for readability reasons). They show that the efficient strengthening for HP nanocomposites is guaranteed by a high dispersion of nanoparticles (low n_a) despite their low A% amount. Conversely,

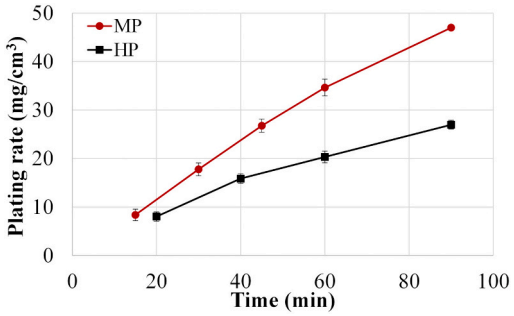

Fig. 10. Plating rate curves for MP and HP depositions.

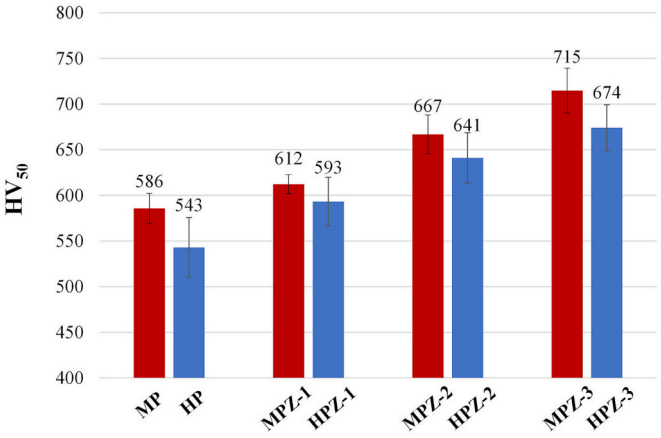

Fig. 11. Comparison of overall microhardness of bare MP, bare HP and nanocomposites reinforced with different amounts of nano-ZrO_2.

dispersion hardening of MP nanocomposites is hampered by the high agglomeration level (high n_a), which limits the strengthening effect associated to the high quantity of embedded nanoparticles (high A%): indeed, presence of big agglomerates decreases the efficiency of Orowan strengthening mechanism [25,27,95] and increases the probability of micro void formation during the co-deposition, thus dramatically reducing the mechanical properties [71,96]. It should be pointed out that such non-uniformity in microhardness properties might affect coatings performances in the expected anti-erosion and anti-wear applications, mostly during the early stages of service life because the worse properties are localized in the outer regions, that are the first to be exposed to environmental attack.

The objective quantification of nanocomposite parameters (i.e. A%, dispersion and distribution of nanoparticles) provides a more comprehensive understanding on how deposition parameters influence nanoparticle incorporation and their effect on coating microhardness. It was demonstrated that introduction of 13.5 g/l of nano-ZrO_2 in HP plating solution allows the production of a uniform nanocomposite with homogenously increased microhardness, combining the well-known corrosion resistance of HP coatings to a higher mechanical strength. Conversely, modification of the plating condition of MP coatings is required to prevent agglomeration issues, which detrimentally affect microhardness. A slower deposition rate can result in a better compromise between incorporation of nanoparticles and agglomeration, ensuing a more uniform distribution of well-dispersed ZrO_2 and higher microhardness improvement.

3.4. Factor influencing microhardness increase

Several authors reported a microhardness increase upon introduction of a higher amount of reinforcing phase, either for ZrO_2 or other hard particles, but only up to a certain threshold beyond which a slight decrease is always registered [38,44,47,66,97]: this behavior was always ascribed to agglomeration issues that, however, were difficult to quantify objectively. The presented results provide evidence that the dispersion hardening effect strongly depends on two parameters: (*i*) the volume fraction of nanoparticles embedded in the coating (measured by A%), as it affect the work-hardening behavior of the material, and (*ii*) agglomeration of the reinforcing phase (estimated by n_a), since it is associated to a lower effectiveness of Orowan mechanism and a greater susceptibility to formation of micro voids that ultimately result in poor mechanical behavior.

The amount and distribution of the embedded particles are crucial aspects in determining the enhancement in mechanical properties of a composite coating. Several authors reported the importance of their combined effect on the mechanical behavior of a nanocomposite material [89,96–98]. Yet, to the authors knowledge, a model to evaluate the mutual effect of the above two features on coating hardness that is based on image analysis is not available in literature.

The presented image analysis routine provides a tool to quantitatively determine A% and agglomeration across coating thickness, enabling the possibility to correlate nanocomposite parameters to

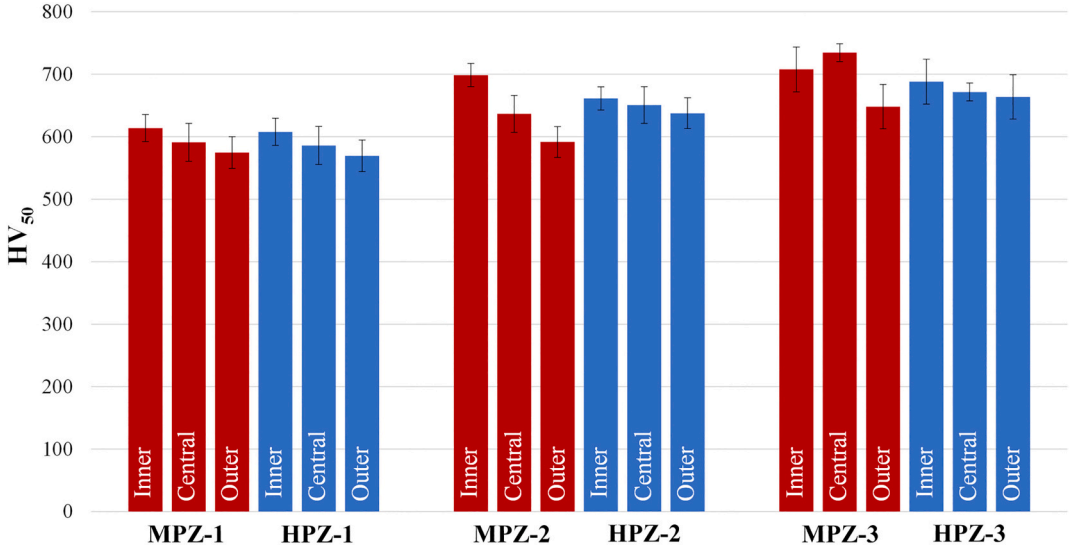

Fig. 12. Comparison of microhardness measured in the inner, central and outer regions of MP and HP nanocomposites reinforced with different amounts of ZrO_2.

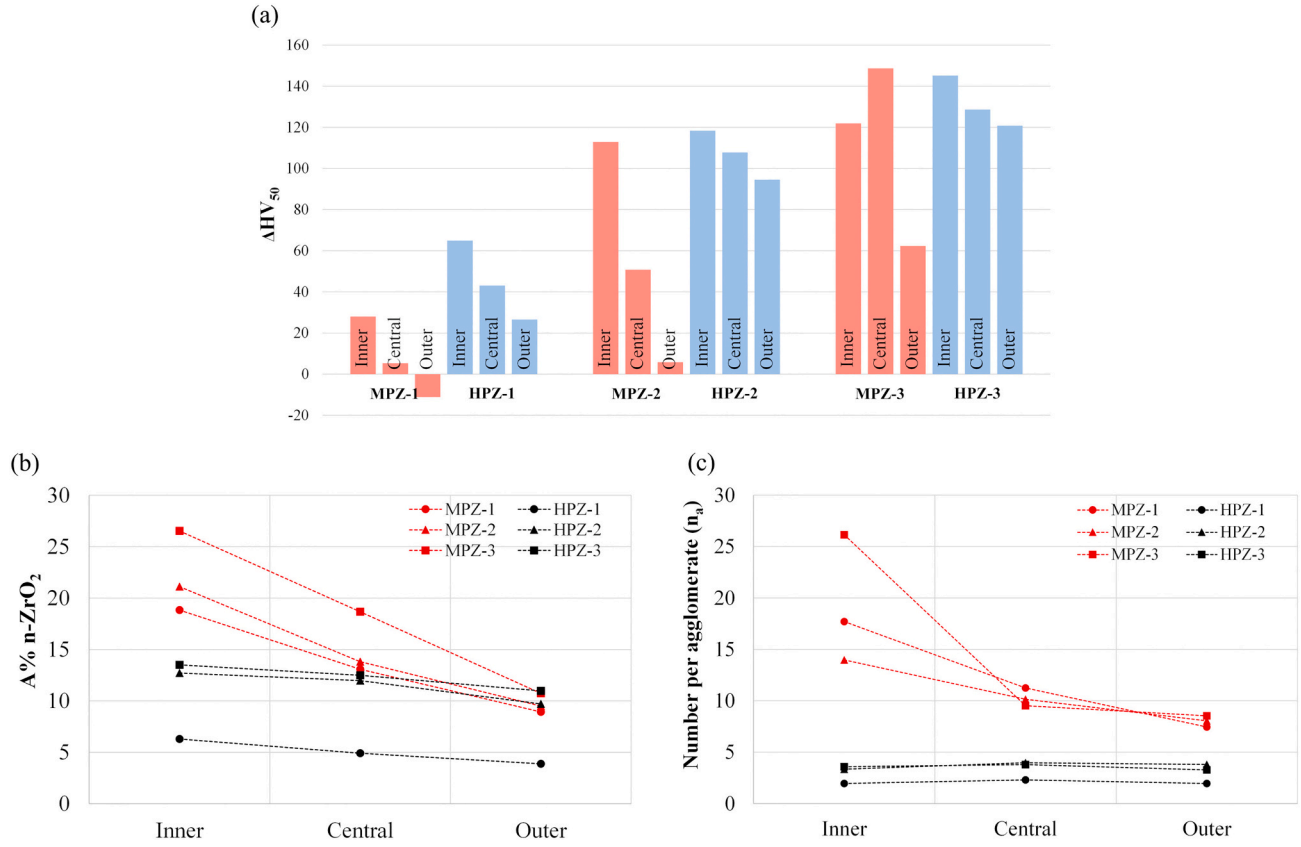

Fig. 13. (a) Relative hardness increase (ΔHV_{50}) measured in the inner, central and outer regions of nanocomposites expressed as increment with respect to bare MP and HP counterpart; (b) A% of embedded ZrO_2 calculated in the inner, central and outer regions of nanocomposite coatings; (c) mean number of particles that constitute an agglomerate (n_a) calculated in the inner, central and outer regions of nanocomposite coatings.

microhardness improvement. The existence of a mathematical relationship $\Delta HV_{50} = f(A\%, n_a)$ was determined using the large dataset available in the present experiments (360 measurement points made by 20 measurements per 3 types of coating, for both MP and HP, on 3 layers). Statistical analysis (by least square method) indicated that a reliable relationship was of simple bilinear form

$$\Delta HV_{50} = 23.1 + 12.9\ A\%,\ -21.4\ n_a + 0.447\ A\% n_a, \quad (3)$$

where coefficients were fit to the presented data.

Fig. 14 shows the result for ΔHV_{50} predicted from the previous formula in comparison with the experimental measurements (showed in gray shade, representing the data of Fig. 13a). The agreement is visually excellent and confirmed by the high correlation coefficient $R_{corr} = 0.96$. The high agreement suggests that the value of ΔHV_{50} can be considered dependent on the two investigated quantities. In confirmation of this, when the same procedure is performed to estimate ΔHV_{50} accounting on A% only, the correlation is substantially reduced ($R_{corr} = 0.45$), while it is negligible as expected ($R_{corr} = 0.024$) when accounting on n_a only.

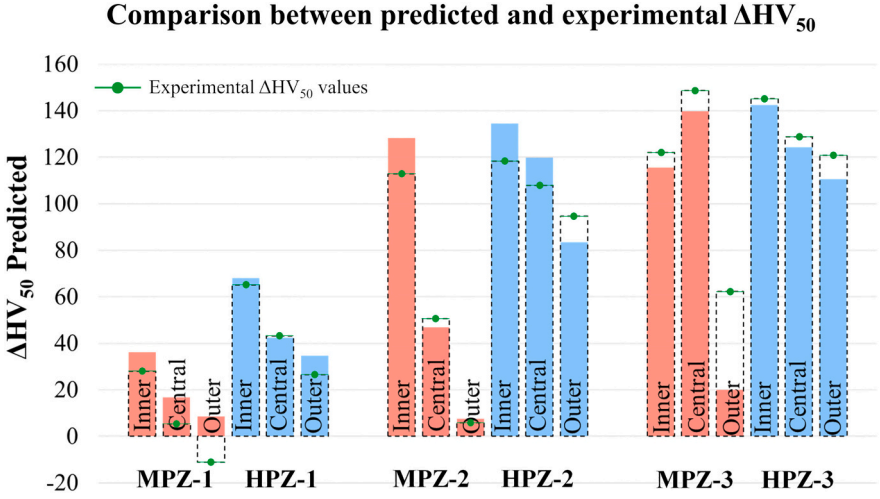

Fig. 14. Comparison between ΔHV_{50} predicted by the bi-linear relation resulted by statistical fitting on the experimental data (colored bars) and experimental measurements (dashed histogram and green markers).

To further confirm the correlation between experimental data and the mathematical bi-linear relation, a new experimental dataset was obtained performing depositions with n-ZrO_2 concentration equal to 16 g/l, out of the previously employed range: the dataset is composed by 90 measurement points made by 10 measurements for one MP and two HP coatings, on 3 layers each coating. Image analysis and particle identification of the new produced coatings is reported in Fig. 15: the large availability of nanoparticles in solution leads to high incorporation, but the produced coatings are highly non-uniform across the thickness. Concentration of nanoparticles is so excessive that they can be barely kept in suspension; deposition is difficult to control over time and parameters, such as agitation, needs to be changed and monitored continuously to mitigate settling and the bottom of the beaker. As a result, the new dataset is very dispersed and obtained triplets of A%, n_a and ΔHV_{50} are reported as red spots in Fig. 16 and superimposed on best fit surface given by Eq. (3). For completeness, the former experimental dataset is reported as blue spots. The correlation coefficient calculated with the new experimental dataset indicates an even better correlation, giving $R_{corr} = 0.98$. Therefore, the strengthening effect upon nanoparticles introduction can be accurately correlated to the combination of the quantity of embedded nanoparticles and the degree of agglomeration, with the main contribution determining the reinforcing capability given by A% and a non-negligible contribution determining the effectiveness of reinforcement that is given by n_a.

The obtained results can provide a useful tool for the optimization of coating properties, allowing the choice of the best deposition parameters leading to maximization of nanocomposite hardness.

3.5. Potentiodynamic polarization test

The effect of P content and incorporation of nano-ZrO_2 on the corrosion resistance of the electroless NiP coatings and nanocomposites was studied by electrochemical method. The potentiodynamic polarization curves of standard MP and HP samples and MPZ-3 and HPZ-3 nanocomposites in 3.5 wt% NaCl solution are reported in Fig. 17. Corresponding corrosion parameters calculated from the Tafel extrapolation method are listed in Table 3.

Comparing MP and HP polarization curves (Fig. 17), it can be observed that corrosion properties are greatly affected by phosphorus content. HP coatings exhibit higher (i.e. more positive) corrosion potential and lower corrosion current density compared with MP ones, thus providing better protection capabilities. Corrosion resistance properties of Ni-P coatings are given by the formation of a phosphorus enriched layer that originates from the preferential dissolution of Ni.

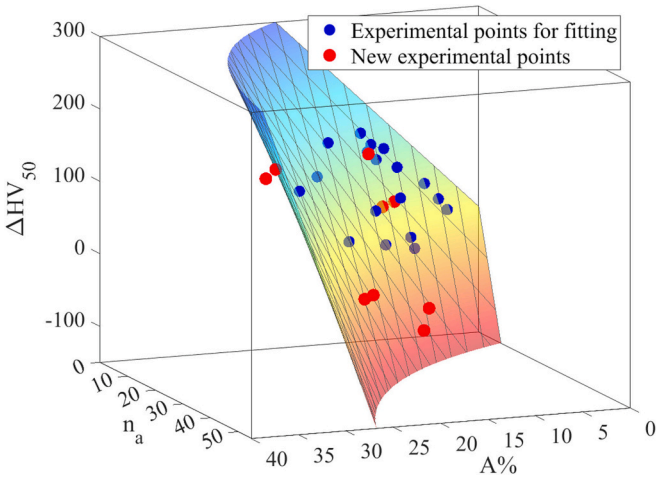

Fig. 16. Comparison between new experimental points (red spots) and former experimental points used for the statistical fitting procedure (blue spots) superimposed on the surface given by the obtained bi-linear relation.

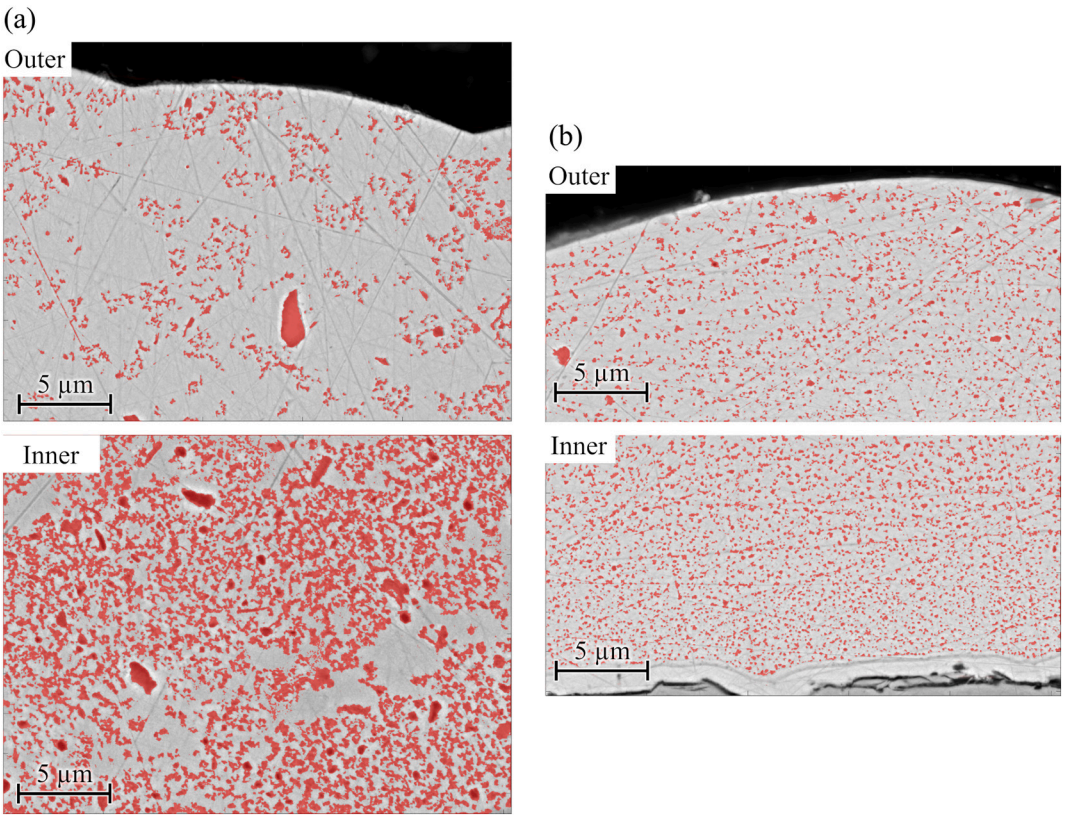

Fig. 15. Routine output of particle identification on LE-BSE SEM micrographs of coatings produced with 16 g/l of nano-ZrO_2: (a) MP nanocomposite, inner and outer region; (b) HP nanocomposite, inner and outer region.

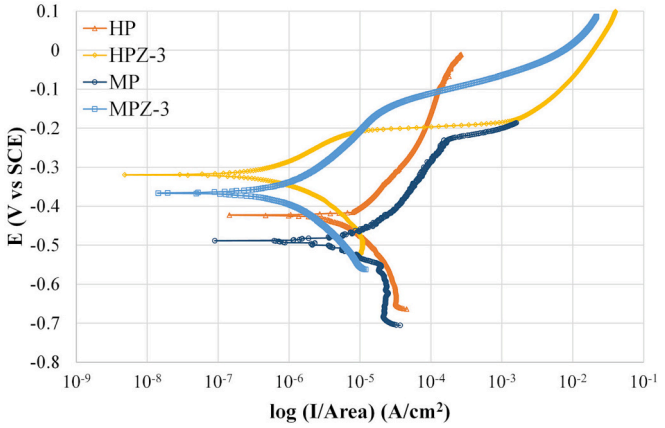

Fig. 17. Potentiodynamic polarization curves of the unreinforced MP and HP coatings and MPZ-3 and HPZ-3 nanocomposites in 3.5 wt% NaCl solution.

Table 3
Corrosion parameters of MP and HP unreinforced Ni-P coatings and MPZ-3 and HPZ-3 nanocomposites.

Sample	E_{corr} (mV vs SCE)	I_{corr} (μA/cm^2)	βa (mV/decade)	βc (mV/decade)	R_p (kΩ·cm^2)
MP	−487.987	3.414	57.35	−91.22	0.127
HP	−423.376	1.608	10.75	−42.05	0.270
MPZ-3	−368.915	0.172	27.742	−35.23	2.518
HPZ-3	−319.138	0.156	30.94	−37.65	2.776

Such concentration of P on the outer part of the surface promotes the formation of stable Ni_3P and Ni_xP_y intermediate compounds, which act as a pseudo-passive barrier film. The enriched P surface also reacts with water to form a layer of adsorbed hypophosphite ions ($H_2PO_2^-$): this layer hinders further penetration of water and corrosive ions towards the surface, preventing the formation of soluble Ni^{2+} compounds and consequent additional Ni dissolution [9,53,99]. Since corrosion resistance of Ni-P alloys is due to the P enrichment at the electrode surface, the initial higher P content of HP coatings determines their superior protective properties compared with MP [10]. Microstructure of coatings is also known to play a role in corrosion resistance. Amorphous microstructure of HP alloys can act as a barrier to the penetration of corrosive agents thanks to the absence of grain boundaries, which form active sites for corrosion attack [16].

Curves in Fig. 17 also demonstrate that both MPZ-3 and HPZ-3 nanocomposites offer better corrosion protection compared with unreinforced coatings. The increased corrosion resistance of ZrO_2 nanocomposites can be ascribed to the reduction of effective metallic area available for corrosion [100]. Similar results of positive shift in the corrosion potential and decrease in corrosion current density after introduction of inert nanoparticles have been widely reported in literature [16,47,50,101]. The improved behavior of nanocomposites also confirms that nanoparticle introduction does not induce defects, porosity or micro-cracking to coatings, making them suitable for applications in aggressive environment.

Tafel corrosion parameters were extrapolated from the region of active dissolution of nickel, where samples undergo uniform corrosion. In that region, corrosion is governed by the diffusion of faster dissolving elements of the alloy through the P-enriched surface and, from the solution side, further penetration of water and corrosive ions is slowed down by the hypophosphite ions ($H_2PO_2^-$) adsorbed on the surface of specimens. Indeed, current density does not show the proper trend of passive corrosion behavior in all investigated samples. Moving towards more positive potentials, all curves show a more rapid increase of the current density. To better understand corrosion behavior, SEM observation and Ferroxyl reagent test were carried out after potentiodynamic polarizations. Surface micrographs in Fig. 18 show intergranular corrosion at the boundary of the nodules in all samples, indicating the onset of localized corrosion. In MP and HP samples, many small cracks can be detected inter-nodulus too, confirming the lower corrosion resistance of these coatings. All specimen where successfully tested negative to the Ferroxyl reagent test after polarizations, thus excluding substrate exposure, except from sample HPZ-3. The local failure of such coatings might explain the current density plateau recorded at potential around −200 mV vs SCE. SEM and EDS observations confirmed the presence of circumscribed substrate exposure and corrosion, as shown in Fig. 19. Nevertheless, it is important to point out that the overall surface of the sample does not show evidence of coating spalling or corrosion by pitting.

4. Conclusions

MP and HP alloy and nanocomposite coatings reinforced with different concentration of nano-ZrO_2 were produced with lead-free and surfactant-free solutions. Reinforcement distribution was quantitatively investigated by analysis of SEM images to identify the effect of different deposition phenomena on the final microhardness.

Both MP and HP coatings display an increased incorporation of nanoparticles with increasing concentration in the plating solution and their introduction doesn't modify neither microstructure nor phosphorus amount. Particle distribution in MP and HP nanocomposites presented significant differences, which could be attributed to the different plating rate of the two depositions. In particular, the faster growth of MP coatings (≈35 μm/h) leads to high incorporation level (high A%) but highly agglomerated reinforcement (high n_a), resulting in a non-uniform distribution of nanoparticles across the thickness. Differently, the slower growth of HP nanocomposites (≈20 μm/h) results in lower A% but a more uniform distribution and lower agglomeration (low n_a). As a result, HP co-deposition led to a more efficient strengthening effect: incorporation of 13.5 A% and agglomeration as low as 4 n_a led to homogeneous hardness improvement up to +145 HV_{50}. Conversely, MP hardening was limited to by the excess of agglomeration, with maximum hardness improvement up to +149 HV_{50} in the central region of MPZ-3 coatings, achieved by 18.7 A% and 10 n_a. The combined effect of A% and n_a on hardness improvement was investigated systematically and a mathematical bi-linear relationship demonstrated that the reinforcing capability is first driven by *A*% with an important contribution on its effectiveness by n_a. Eventually, potentiodynamic polarization test demonstrated that introduction of ZrO_2 nanoparticles enhances corrosion resistance of both MP and HP coatings. The presented strategy for optimization of coating properties can provide a simple and effective method to increase the resistance of engineering components for anti-wear/erosion applications in corrosive environment, such as midstream and downstream service in the energy production industry.

CRediT authorship contribution statement

Giulia Pedrizzetti: Conceptualization, Methodology, Software, Investigation, Formal analysis, Writing – original draft. **Laura Paglia:** Conceptualization, Investigation, Methodology, Data curation. **Virgilio Genova:** Validation, Investigation, Visualization, Writing – review & editing. **Serena Cinotti:** Resources, Validation, Supervision. **Michelangelo Bellacci:** Resources, Validation, Supervision. **Francesco Marra:** Supervision, Validation, Writing – review & editing, Funding acquisition. **Giovanni Pulci:** Conceptualization, Project administration, Writing – review & editing, Funding acquisition.

Declaration of competing interest

The authors declare that they have no known competing financial interests or personal relationships that could have appeared to influence the work reported in this paper.

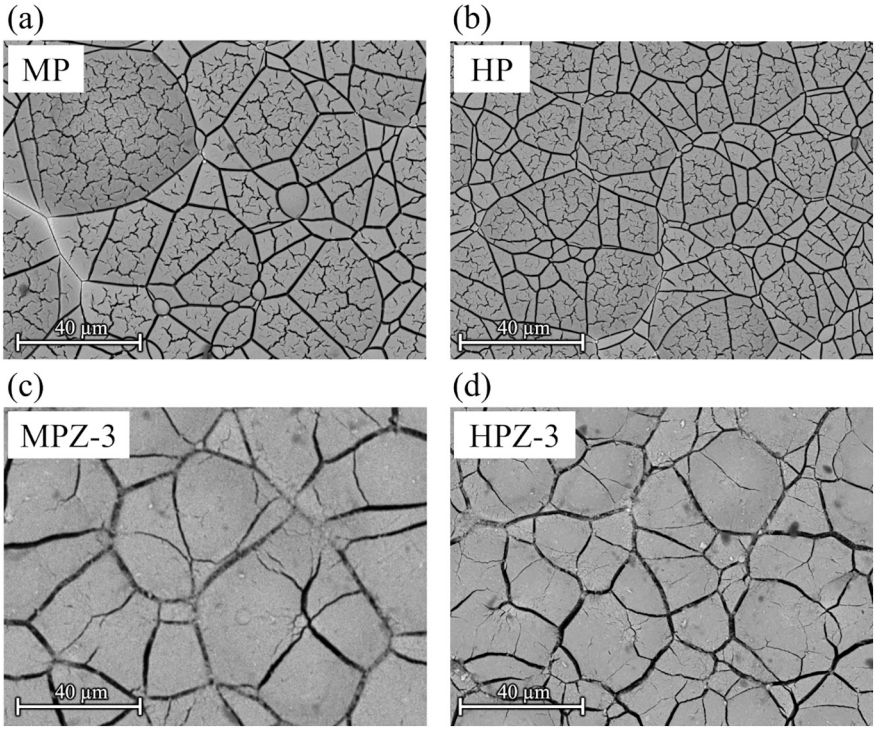

Fig. 18. Surface BSE-SEM micrographs of MP (a), HP (b), MPZ-3 (c) and HPZ-3 (d) coatings after potentiodynamic polarizations.

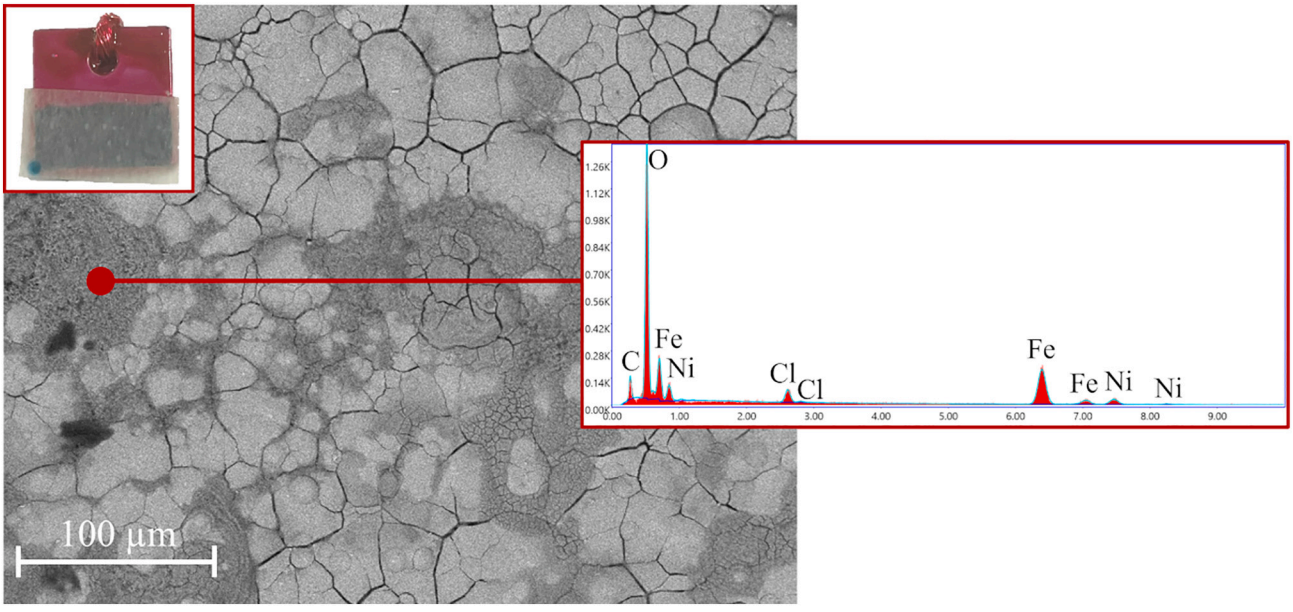

Fig. 19. BSE-SEM surface micrograph of HPZ-3 sample after potentiodynamic polarization test in the region of substrate exposure EDS analysis reveals occurrence substrate corrosion. Insert shows the result of Ferroxyl reagent test, with substrate exposure located on the low-left edge of the specimen.

Data availability

Data will be made available on request.

Acknowledgements

The authors acknowledge the financial support by Baker Hughes (Nuovo Pignone Tecnologie, Florence, Italy).

References

[1] D.W. Baudrand, Electroless nickel plating, in: C.M. Cotell, J.A. Sprague, F.A. J. Smidt (Eds.), ASM Metal Handbook Volume 5 - Surface Engineering, ASM International, 1994.
[2] K.H. Krishnan, S. John, K.N. Srinivasan, J. Praveen, M. Ganesan, P.M. Kavimani, An overall aspect of electroless Ni-P depositions-a review article, Metall. Mater. Trans. A 37A (2006).
[3] H.-J. Alfort, When does the ban on chromium (VI) come into effect? Int. Surf. Technol. 1 (2017) 48–51.
[4] L. Xu, L. Pi, Y. Dou, Y. Cui, X. Mao, A. Lin, C. Fernandez, C. Peng, Electroplating of thick hard chromium coating from a trivalent chromium bath containing a

ternary complexing agent: a methodological and mechanistic study, ACS Sustain. Chem. Eng. 8 (2020) 15540–15549.
[5] S. Mahdavi, S.R. Allahkaram, A. Heidarzadeh, Characteristics and properties of Cr coatings electrodeposited from Cr(III) baths, Mater. Res. Express 6 (2019), https://doi.org/10.1088/2053-1591/aaeb4f.
[6] M.S. Alam, A.K. Das, Advancement in cermet based coating on steel substrate: a review, Mater Today Proc. 56 (2022) 805–810, https://doi.org/10.1016/j.matpr.2022.02.260.
[7] K. Torkashvand, S. Joshi, V. Testa, F. Ghisoni, S. Morelli, G. Bolelli, L. Lusvarghi, F. Marra, M. Gupta, Tribological behavior of HVAF-sprayed WC-based coatings with alternative binders, Surf. Coat. Technol. 436 (2022), https://doi.org/10.1016/j.surfcoat.2022.128296.
[8] A. Lelevic, F.C. Walsh, Electrodeposition of Ni-P alloy coatings: a review, Surf. Coat. Technol. 369 (2019) 198–220, https://doi.org/10.1016/j.surfcoat.2019.03.055.
[9] P. Sahoo, S.K. Das, Tribology of electroless nickel coatings - a review, Mater. Des. 32 (2011) 1760–1775, https://doi.org/10.1016/j.matdes.2010.11.013.
[10] T.S.N. Sankara Narayanan, I. Baskaran, K. Krishnaveni, S. Parthiban, Deposition of electroless Ni-P graded coatings and evaluation of their corrosion resistance, Surf. Coat. Technol. 200 (2006) 3438–3445, https://doi.org/10.1016/j.surfcoat.2004.10.014.
[11] G.O. Mallory, J.B., Hajdu, Electroless Plating: Fundamentals and Applications, American Electroplaters and Surface Finishers Society, 1990.
[12] J.N. Balaraju, T.S.N. Sankara Narayanan, S.K. Seshadri, Structure and phase transformation behaviour of electroless Ni-P composite coatings, Mater. Res. Bull. 41 (2006) 847–860, https://doi.org/10.1016/j.materresbull.2005.09.024.
[13] A.J. Gould, P.J. Boden, S.J. Harris, Phosphorus distribution in electroless nickel deposits, Surf. Technol. 12 (1981) 93–102.
[14] K.G. Keong, W. Sha, S. Malinov, Crystallisation kinetics and phase transformation behaviour of electroless nickel-phosphorus deposits with high phosphorus content, J. Alloys Compd. 334 (2002) 192–199. www.elsevier.com/locate/jallcom.
[15] A.H. Graham, R.W. Lindsay, H.J. Read, Structure of electroless nickel, J. Electrochem. Soc. 109 (1962).
[16] E.M. Fayyad, A.M. Abdullah, M.K. Hassan, A.M. Mohamed, G. Jarjoura, Z. Farhat, Recent advances in electroless-plated Ni-P and its composites for erosion and corrosion applications: a review, Emerg. Mater. 1 (2018) 3–24, https://doi.org/10.1007/s42247-018-0010-4.
[17] D. Dong, X.H. Chen, W.T. Xiao, G.B. Yang, P.Y. Zhang, Preparation and properties of electroless Ni-P-SiO 2 composite coatings, Appl. Surf. Sci. 255 (2009) 7051–7055, https://doi.org/10.1016/j.apsusc.2009.03.039.
[18] M.-D. Ger, B.J. Hwang, Effect of surfactants on codeposition of PTFE particles with electroless Ni-P coating, Mater. Chem. Phys. 76 (2002) 38–45.
[19] J.N. Balaraju, T.S.N. Sankara Narayanan, S.K. Seshadri, Electroless Ni-P composite coatings, J. Appl. Electrochem. 33 (2003) 807–816.
[20] J. Sudagar, J. Lian, W. Sha, Electroless nickel, alloy, composite and nano coatings - a critical review, J. Alloys Compd. 571 (2013) 183–204, https://doi.org/10.1016/j.jallcom.2013.03.107.
[21] N.P. Wasekar, L. Bathini, L. Ramakrishna, D.S. Rao, G. Padmanabham, Pulsed electrodeposition, mechanical properties and wear mechanism in Ni-W/SiC nanocomposite coatings used for automotive applications, Appl. Surf. Sci. 527 (2020), https://doi.org/10.1016/j.apsusc.2020.146896.
[22] I. Shao, P.M. Vereecken, C.L. Chien, P.C. Searson, R.C. Cammarata, Synthesis and characterization of particle-reinforced Ni/Al2O3 nanocomposites, J. Mater. Res. 17 (2002) 1412–1418.
[23] P.M. Hazzledine, N.P. Nouat, Direct as against indirect dispersion work hardening, Philos. Mag. Lett. 70 (1994) 129–133, https://doi.org/10.1080/09500839408240965.
[24] S. Pinate, E. Ghassemali, C. Zanella, Strengthening mechanisms and wear behavior of electrodeposited Ni–SiC nanocomposite coatings, J. Mater. Sci. 57 (2022) 16632–16648, https://doi.org/10.1007/s10853-022-07655-1.
[25] Z. Zhang, D.L. Chen, Contribution of Orowan strengthening effect in particulate-reinforced metal matrix nanocomposites, Mater. Sci. Eng. A 483–484 (2008) 148–152, https://doi.org/10.1016/j.msea.2006.10.184.
[26] Z. Zhang, D.L. Chen, Consideration of Orowan strengthening effect in particulate-reinforced metal matrix nanocomposites: a model for predicting their yield strength, Scr. Mater. 54 (2006) 1321–1326, https://doi.org/10.1016/j.scriptamat.2005.12.017.
[27] I. Apachitei, F.D. Tichelaar, J. Duszczyk, L. Katgerman, The effect of heat treatment on the structure and abrasive wear resistance of autocatalytic NiP and NiP-SiC coatings, Surf. Coat. Technol. 149 (2002) 263–278.
[28] M. Ram, A. Ansari, S. Sharma, A.K. Sharma, Annealing effect on tribological resistance of electroless Ni-P/SiC nanocomposite coatings, in: AIP Conf Proc, American Institute of Physics Inc., 2020, https://doi.org/10.1063/5.0030146.
[29] M. Khodaei, A.M. Gholizadeh, SiC nanoparticles incorporation in electroless NiP-graphene oxide nanocomposite coatings, Ceram. Int. 47 (2021) 25287–25295, https://doi.org/10.1016/j.ceramint.2021.05.250.
[30] S. Kumar, R. Goli, S.K. Ghosh, Performance analysis of SiC-Ni-P nanocomposite electroless coated brake pad, Mater. Manuf. Process. 37 (2022) 764–781, https://doi.org/10.1080/10426914.2021.1981932.
[31] K. Czapczyk, P. Zawadzki, N. Wierzbicka, R. Talar, Microstructure and properties of electroless ni-p/si3n4 nanocomposite coatings deposited on the aw-7075 aluminum alloy, Materials 14 (2021), https://doi.org/10.3390/ma14164487.
[32] D.R. Dhakal, Y.K. Kshetri, G. Gyawali, T.H. Kim, J.H. Choi, S.W. Lee, Understanding the effect of Si3N4 nanoparticles on wear resistance behavior of electroless nickel-phosphorus coating through structural investigation, Appl. Surf. Sci. 541 (2021), https://doi.org/10.1016/j.apsusc.2020.148403.
[33] S. Karthikeyan, B. Ramamoorthy, Effect of reducing agent and nano Al2O3 particles on the properties of electroless Ni-P coating, Appl. Surf. Sci. 307 (2014) 654–660, https://doi.org/10.1016/j.apsusc.2014.04.092.
[34] M. Novák, D. Vojtěch, T. Vítů, Influence of heat treatment on tribological properties of electroless Ni-P and Ni-P-Al2O3 coatings on Al-Si casting alloy, Appl. Surf. Sci. 256 (2010) 2956–2960, https://doi.org/10.1016/j.apsusc.2009.11.057.
[35] A. Arumugam, P. Lakshmanan, S. Palani, K. Parthiban, Wear behavior of Ni-P and Al2O3electroless nano coating on aluminium alloy, in: Mater Today Proc, Elsevier Ltd, 2021, pp. 1066–1070, https://doi.org/10.1016/j.matpr.2021.01.425.
[36] S. Amjad-Iranagh, M. Zarif, TiO2 nano-particle effect on the chemical and physical properties of Ni-P-TiO2 nanocomposite electroless coatings, J. Nanostruct. 10 (2020) 415–423, https://doi.org/10.22052/JNS.2020.02.019.
[37] I. Saravanan, A. Elayaperumal, A. Devaraju, M. Karthikeyan, A. Raji, Wear behaviour of electroless Ni-P and Ni-P-TiO2 composite coatings on En8 steel, in: Mater Today Proc, Elsevier Ltd, 2020, pp. 1135–1139, https://doi.org/10.1016/j.matpr.2019.12.007.
[38] J. Novakovic, P. Vassiliou, K. Samara, T. Argyropoulos, Electroless NiP-TiO2 composite coatings: their production and properties, Surf. Coat. Technol. 201 (2006) 895–901, https://doi.org/10.1016/j.surfcoat.2006.01.005.
[39] L. Yu, W. Huang, X. Zhao, Preparation and characterization of Ni-P-nanoTiN electroless composite coatings, J. Alloys Compd. 509 (2011) 4154–4159, https://doi.org/10.1016/j.jallcom.2011.01.025.
[40] B. Chen, F. Yan, J. Guo, M.F. Yan, Y. Zhang, Attractive effects of Re on electroless Ni-P-TiN nanocomposite coating, Appl. Surf. Sci. 565 (2021), https://doi.org/10.1016/j.apsusc.2021.150472.
[41] M. Farhan, O. Fayyaz, M. Nawaz, A.B. Radwan, R.A. Shakoor, Synthesis and properties of electroless Ni–P-HfC nanocomposite coatings, Mater. Chem. Phys. 291 (2022), https://doi.org/10.1016/j.matchemphys.2022.126696.
[42] M. Dehestani, E. Adolfsson, Phase stability and mechanical properties of zirconia and zirconia composites, Int. J. Appl. Ceram. Technol. 10 (2013) 129–141, https://doi.org/10.1111/j.1744-7402.2011.02717.x.
[43] K. Zielińska, A. Stankiewicz, I. Szczygieł, Electroless deposition of Ni-P-nano-ZrO 2 composite coatings in the presence of various types of surfactants, J. Colloid Interface Sci. 377 (2012) 362–367, https://doi.org/10.1016/j.jcis.2012.03.049.
[44] P.A. Gay, J.M. Limat, P.A. Steinmann, J. Pagetti, Characterisation and mechanical properties of electroless NiP-ZrO2 coatings, Surf. Coat. Technol. 202 (2007) 1167–1171, https://doi.org/10.1016/j.surfcoat.2007.05.081.
[45] Y.W. Song, D.Y. Shan, R.S. Chen, E.H. Han, Study on electroless Ni-P-ZrO2 composite coatings on AZ91D magnesium alloys, Surf. Eng. 23 (2007) 334–338, https://doi.org/10.1179/174329406X150422.
[46] P. Makkar, D.D. Mishra, R.C. Agarwala, V. Agarwala, A novel electroless plating of Ni-P-Al-ZrO2 nanocomposite coatings and their properties, Ceram. Int. 40 (2014) 12013–12021, https://doi.org/10.1016/j.ceramint.2014.04.040.
[47] S.M.A. Shibli, K.S. Chinchu, M.A. Sha, Development of nano-tetragonal zirconia-incorporated Ni–P coatings for high corrosion resistance, Acta Metall. Sin. (Engl. Lett.) 32 (2019) 481–494, https://doi.org/10.1007/s40195-018-0823-4.
[48] M.H. Sliem, K. Shahzad, V.N. Sivaprasad, R.A. Shakoor, A.M. Abdullah, O. Fayyaz, R. Kahraman, M.A. Umer, Enhanced mechanical and corrosion protection properties of pulse electrodeposited NiP-ZrO2 nanocomposite coatings, Surf. Coat. Technol. 403 (2020), https://doi.org/10.1016/j.surfcoat.2020.126340.
[49] M.H. Sliem, O. Fayyaz, R.A. Shakoor, S. Bagheridard, B. Mansoor, A. Abdullah, A. M.A. Mohamed, The influence of different preparation methods on the erosion behavior of NiP-ZrO2 nanocomposite coating, Tribol. Int. 178 (2023), https://doi.org/10.1016/j.triboint.2022.108014.
[50] Y. He, S. Zhang, Y. He, R. Song, Z. Zhang, B. Liu, H. Li, J. Shangguan, Effects of yttrium-stabilized zirconia (different yttrium content) doping on the structure, corrosion resistance and wear resistance of Ni-P electroless coating, Colloids Surf. A Physicochem. Eng. Asp. 654 (2022), https://doi.org/10.1016/j.colsurfa.2022.130059.
[51] V.B. Chintada, T.R. Gurugubelli, R. Koutavarapu, The impact of surfactants on the properties of electroless Ni–P–SiC coatings, Mater. Chem. Phys. 291 (2022), https://doi.org/10.1016/j.matchemphys.2022.126682.
[52] E.M. Fayyad, A.M. Abdullah, A.M.A. Mohamed, G. Jarjoura, Z. Farhat, M. K. Hassan, Effect of electroless bath composition on the mechanical, chemical, and electrochemical properties of new NiP–C 3 N 4 nanocomposite coatings, Surf. Coat. Technol. 362 (2019) 239–251, https://doi.org/10.1016/j.surfcoat.2019.01.087.
[53] M. Khodaei, A.M. Gholizadeh, Surfactant-free commercial electroless bath with low concentration of SiC nanoparticles to prepare the NiP-SiC nanocomposite coatings, Mater. Res. Express 8 (2021), https://doi.org/10.1088/2053-1591/ac021e.
[54] B. Bozzini, P.L. Cavallotti, G. Giovannelli, B. Brevaglieri, S. Natali, Quantitaive metallography and image analysis of composite coatings obtained by autocatalytic chemical deposition, Pract. Metallogr. 33 (1996) 130–145.
[55] S. Alirezaei, S.M. Monirvaghefi, M. Salehi, A. Saatchi, Effect of alumina content on surface morphology and hardness of Ni-P-Al2O3(α) electroless composite coatings, Surf. Coat. Technol. 184 (2004) 170–175, https://doi.org/10.1016/j.surfcoat.2003.11.013.
[56] S.L. Kuo, Y.C. Chen, M. Der Ger, W.H. Hwu, Nano-particles dispersion effect on Ni/Al2O3 composite coatings, Mater. Chem. Phys. 86 (2004) 5–10, https://doi.org/10.1016/j.matchemphys.2003.11.040.

[57] A. Góral, Nanoscale structural defects in electrodeposited Ni/Al2O3 composite coatings, Surf. Coat. Technol. 319 (2017) 23–32, https://doi.org/10.1016/j.surfcoat.2017.03.061.

[58] H.H. Sheu, P.C. Huang, L.C. Tsai, K.H. Hou, Effects of plating parameters on the Ni-P-Al2O3 composite coatings prepared by pulse and direct current plating, Surf. Coat. Technol. 235 (2013) 529–535, https://doi.org/10.1016/j.surfcoat.2013.08.020.

[59] H. Shahbazi, M. Mahdavi, S. Alirezaei, F. Tabatabaei, Corrosion behavior of Ni-P-Ag and Ni-P-Al2O3 composite coatings Ni-P-Ag and Ni-P-Al2O3 composite, Mater. Res. Express 6 (2019), https://doi.org/10.1088/2053-1591/ab1fcd/meta.

[60] C.F. Malfatti, H.M. Veit, T.L. Menezes, J. Zoppas Ferreira, J.S. Rodriguês, J. P. Bonino, The surfactant addition effect in the elaboration of electrodepositated NiP-SiC composite coatings, Surf. Coat. Technol. 201 (2007) 6318–6324, https://doi.org/10.1016/j.surfcoat.2006.11.040.

[61] N.P. Wasekar, S.M. Latha, M. Ramakrishna, D.S. Rao, G. Sundararajan, Pulsed electrodeposition and mechanical properties of Ni-W/SiC nano-composite coatings, Mater. Des. 112 (2016) 140–150, https://doi.org/10.1016/j.matdes.2016.09.070.

[62] Y.T.R. Lee, H. Ashrafizadeh, G. Fisher, A. McDonald, Effect of type of reinforcing particles on the deposition efficiency and wear resistance of low-pressure cold-sprayed metal matrix composite coatings, Surf. Coat. Technol. 324 (2017) 190–200, https://doi.org/10.1016/j.surfcoat.2017.05.057.

[63] U. Matik, Structural and wear properties of heat-treated electroless Ni-P alloy and Ni-P-Si3N4 composite coatings on iron based PM compacts, Surf. Coat. Technol. 302 (2016) 528–534, https://doi.org/10.1016/j.surfcoat.2016.06.054.

[64] C.I. Hsu, K.H. Hou, M. Der Ger, G.L. Wang, The effect of incorporated self-lubricated BN(h) particles on the tribological properties of Ni-P/BN(h) composite coatings, Appl. Surf. Sci. 357 (2015) 1727–1735, https://doi.org/10.1016/j.apsusc.2015.09.207.

[65] M.K. Das, R. Li, J. Qin, X. Zhang, K. Das, A. Thueploy, S. Limpanart, Y. Boonyongmaneerat, M. Ma, R. Liu, Effect of electrodeposition conditions on structure and mechanical properties of Ni-W/diamond composite coatings, Surf. Coat. Technol. 309 (2017) 337–343, https://doi.org/10.1016/j.surfcoat.2016.11.074.

[66] X. Shu, Y. Wang, C. Liu, A. Aljaafari, W. Gao, Double-layered Ni-P/Ni-P-ZrO2 electroless coatings on AZ31 magnesium alloy with improved corrosion resistance, Surf. Coat. Technol. 261 (2015) 161–166, https://doi.org/10.1016/j.surfcoat.2014.11.040.

[67] M. Sabzi, S.M. Dezfuli, Z. Balak, Crystalline texture evolution, control of the tribocorrosion behavior, and significant enhancement of the abrasion properties of a Ni-P nanocomposite coating enhanced by zirconia nanoparticles, Int. J. Miner. Metall. Mater. 26 (2019) 1020–1030, https://doi.org/10.1007/s12613-019-1805-x.

[68] I. Apachitei, J. Duszczyk, Autocatalytic nickel coatings on aluminium with improved abrasive wear resistance, Surf. Coat. Technol. 132 (2000) 89–98.

[69] D.B. Williams, R. Michael, I. Goldstem, A.D. Romlg, Definition of the spatial resolution of X-ray microanalysis in thin foils, Ultramicroscopy 47 (1992) 121–132.

[70] American Society for Testing and Materials, ASTM G59–97, Standard Test Method for Conducting Potentiodynamic Polarization Resistance Measurements, 2014.

[71] N. Ghavidel, S.R. Allahkaram, R. Naderi, M. Barzegar, H. Bakhshandeh, Corrosion and wear behavior of an electroless Ni-P/nano-SiC coating on AZ31 Mg alloy obtained through environmentally-friendly conversion coating, Surf. Coat. Technol. 382 (2020), https://doi.org/10.1016/j.surfcoat.2019.125156.

[72] B. Farber, E. Cadel, A. Menand, G. Schmitz, R. Kirchheim, Phosphorus segregation in nanocrystalline Ni-3.6 at.% P alloy investigated with the tomographic atom probe (TAP), Acta Mater. 48 (2000) 789–796. www.elsevier.com/locate/actamat.

[73] A. Farzaneh, M. Mohammadi, M. Ehteshamzadeh, F. Mohammadi, Electrochemical and structural properties of electroless Ni-P-SiC nanocomposite coatings, Appl. Surf. Sci. 276 (2013) 697–704, https://doi.org/10.1016/j.apsusc.2013.03.156.

[74] R.C. Agarwala, V. Agarwala, Electroless alloy/composite coatings: a review, Sadhana 28 (2003) 475–493.

[75] S. Samanta, K. Vishwanath, K. Mondal, M. Dutta, S.B. Singh, Electroless amorphous NiP coatings over API X70 steel: resistance to wear and hydrogen embrittlement, Met. Mater. Int. 28 (2022) 397–411, https://doi.org/10.1007/s12540-021-01102-7.

[76] C.A. Vlaic, M. Kurniawan, R. Peipmann, C.C. Lalău, M. Stich, U. Schmidt, A. Bund, Improved wear resistance of alternating amorphous and crystalline layers in electrodeposited Ni-P multilayers, Surf. Coat. Technol. 386 (2020), https://doi.org/10.1016/j.surfcoat.2020.125470.

[77] M. Sarret, C. Müller, A. Amell, Electroless NiP micro- and nano-composite coatings, Surf. Coat. Technol. 201 (2006) 389–395, https://doi.org/10.1016/j.surfcoat.2005.11.127.

[78] Y.Y. Liu, J. Yu, H. Huang, B.H. Xu, X.L. Liu, Y. Gao, X.L. Dong, Synthesis and tribological behavior of electroless Ni-P-WC nanocomposite coatings, Surf. Coat. Technol. 201 (2007) 7246–7251, https://doi.org/10.1016/j.surfcoat.2007.01.035.

[79] A. Salicio-Paz, I. Ugarte, J. Sort, E. Pellicer, E. García-Lecina, Full optimization of an electroless nickel solution: boosting the performance of low-phosphorous coatings, Materials 14 (2021), https://doi.org/10.3390/ma14061501.

[80] S.M.A. Shibli, V.S. Dilimon, T. Deepthi, ZrO2-reinforced Ni-P plate: an effective catalytic surface for hydrogen evolution, Appl. Surf. Sci. 253 (2006) 2189–2195, https://doi.org/10.1016/j.apsusc.2006.04.025.

[81] F. Tabatabaei, S. Vardak, S. Alirezaei, K. Raeissi, The tribocorrosion behavior of Ni-P and Ni-P-ZrO2 coatings, Kovove Mater. 56 (2018) 379–387, https://doi.org/10.4149/km.

[82] K.S. Chinchu, A.H. Riyas, M. Ameen Sha, C.v. Geethanjali, V.S. Saji, S.M.A. Shibli, ZrO2–CeO2 assimilated electroless Ni–P anti-corrosion coatings, Surf. Interfaces 21 (2020), https://doi.org/10.1016/j.surfin.2020.100704.

[83] B.W. Zhang, S.Z. Liao, H.W. Xie, H. Zhang, Progress of electroless amorphous and nano alloy deposition: a review - part 2, Trans. Inst. Met. Finish. 92 (2014) 74–80, https://doi.org/10.1179/0020296714Z.000000000168.

[84] N. Feldstein, P.R. Amodio, Anionic inhibition in electroless plating, J. Electrochem. Soc. 117 (1070) 1110–1113.

[85] W.J. Cheong, B.L. Luan, D.W. Shoesmith, The effects of stabilizers on the bath stability of electroless Ni deposition and the deposit, Appl. Surf. Sci. 229 (2004) 282–300, https://doi.org/10.1016/j.apsusc.2004.02.003.

[86] W.-W. Chen, W. Gao, Microstructures and properties of sol-enhanced nanostructured metal-oxide composite coatings, Prog. Nat. Sci.: Mater. Int. 21 (2011) 355–362.

[87] K. Hou, L. Wang, S. Ke, The wear behaviour of electro-codeposited Ni-SiC composites, Wear 253 (2002) 994–1003.

[88] M. der Ger, Electrochemical deposition of nickel/SiC composites in the presence of surfactants, Mater. Chem. Phys. 87 (2004) 67–74, https://doi.org/10.1016/j.matchemphys.2004.04.022.

[89] D. Ahmadkhaniha, C. Zanella, The effects of additives, particles load and current density on codeposition of SiC particles in NiP nanocomposite coatings, Coatings 9 (2019), https://doi.org/10.3390/coatings9090554.

[90] Y. Yang, W. Chen, C. Zhou, H. Xu, W. Gao, Fabrication and characterization of electroless Ni–P–ZrO2 nano-composite coatings, Appl. Nanosci. (Switzerland) 1 (2011) 19–26, https://doi.org/10.1007/s13204-011-0003-6.

[91] Y. Wang, X. Shu, S. Wei, C. Liu, W. Gao, R.A. Shakoor, R. Kahraman, Duplex Ni-P-ZrO2/Ni-P electroless coating on stainless steel, J. Alloys Compd. 630 (2015) 189–194, https://doi.org/10.1016/j.jallcom.2015.01.064.

[92] I.R. Mafi, C. Dehghanian, Comparison of the coating properties and corrosion rates in electroless Ni-P/PTFE composites prepared by different types of surfactants, Appl. Surf. Sci. 257 (2011) 8653–8658, https://doi.org/10.1016/j.apsusc.2011.05.043.

[93] D.L. Sahagian, A.A. Proussevitch, 3D particle size distributions from 2D observations: stereology for natural applications, J. Volcanol. Geotherm. Res. 84 (1998) 173–196.

[94] J. Schiotz, T. Vegge, F.D. Di Tolla, K.W. Jacobsen, Atomic-scale simulations of the mechanical deformation of nanocrystalline metals, Phys. Rev. B 60 (1999) 11971–11983.

[95] H. Algul, M. Uysal, A. Alp, A comparative study on morphological, mechanical and tribological properties of electroless NiP, NiB and NiBP coatings, Appl. Surf. Sci. Adv. 4 (2021), https://doi.org/10.1016/j.apsadv.2021.100089.

[96] B. Bakhit, A. Akbari, Effect of particle size and co-deposition technique on hardness and corrosion properties of Ni-Co/SiC composite coatings, Surf. Coat. Technol. 206 (2012) 4964–4975, https://doi.org/10.1016/j.surfcoat.2012.05.122.

[97] S. Sadreddini, Z. Salehi, H. Rassaie, Characterization of Ni-P-SiO 2 nano-composite coating on magnesium, Appl. Surf. Sci. 324 (2015) 393–398, https://doi.org/10.1016/j.apsusc.2014.10.144.

[98] K. Niihara, A. Nakihara, Strengthening and toughening mechanisms in nanocomposite ceramics, Ann. Chim. Fr. 16 (1991) 479–486.

[99] B. Elsener, M. Crobu, M.A. Scorciapino, A. Rossi, Electroless deposited Ni-P alloys: corrosion resistance mechanism, J. Appl. Electrochem. 38 (2008) 1053–1060, https://doi.org/10.1007/s10800-008-9573-8.

[100] F. Bigdeli, S.R. Allahkaram, An investigation on corrosion resistance of as-applied and heat treated Ni-P/nanoSiC coatings, Mater. Des. 30 (2009) 4450–4453, https://doi.org/10.1016/j.matdes.2009.04.020.

[101] I.A. Shozib, A. Ahmad, A.M. Abdul-Rani, M. Beheshti, A.A. Aliyu, A review on the corrosion resistance of electroless Ni-P based composite coatings and electrochemical corrosion testing methods, Corros. Rev. 40 (2022) 1–37, https://doi.org/10.1515/corrrev-2020-0091.